Fabrication and Characterization of Photolithographically Patterned Rough Surfaces Demonstrating Extreme Contact Angle Behavior

by

Brendan Koch

A thesis submitted in partial fulfillment of the requirements for the degree of

Master of Science

Department of Mechanical Engineering

University of Alberta

Abstract

This thesis features experimental work done to fabricate and characterize silicon surfaces patterned using photolithographic techniques, both standard and novel, to produce a variety of surfaces with roughness of controlled geometric properties. In specific, one set of the surfaces fabricated had pillars with vertical sidewalls to explore the effects of feature size on contact angle, and another set of surfaces had pillars with undercut geometry to test for superoleophobicity. Contact angles were measured on these surfaces using three different test fluids: water, ethylene glycol, and hexadecane. This allowed for a broad range of surface tensions to be examined and thus for a variety of behaviors to be observed during characterization. In analyzing the data new complexities already seen in the literature but not fully explored became apparent. In order to understand these complexities a new framework was developed to empirically describe how liquids behave on rough surfaces such as the ones that were fabricated. This new framework has provided considerable insight and has greatly improved understanding of the behavior of contact angles on the fabricated surfaces and other surfaces in the literature. The framework has allowed us to better understand how drops on textured surfaces behave and how measurements relate to various methods of understanding contact angles, such as the Cassie and Wenzel equations. This is particularly important when assessing surfaces with novel texturing features such as the overhanging cap structure and comparing their behaviors with that of surfaces better characterized in the literature such as surfaces with vertical sidewall pillars, and being able to more accurately and precisely determine what the strengths and weaknesses of these new surfaces really are.

Preface

Chapter 2 of this thesis, with minor modifications has been accepted for publication in the Journal of Physical Chemistry C, as B. M. L. Koch, A. Amirfazli, J.A.W. Elliott, “Modeling and Measurement of Contact Angle Hysteresis on Textured High-Contact-Angle Surfaces” In Press 2014**.**

Chapter 3 of this thesis, with minor modifications, has been accepted for publication to the Journal of Physical Chemistry C, as B. M. L. Koch, A. Amirfazli, J.A.W. Elliott, “Wetting of Rough Surfaces by a Low Surface Tension Liquid”**.**

Chapter 4 of this thesis, with minor modifications, has been submitted for publication to Langmuir as B. M. L. Koch, A. Amirfazli, J.A.W. Elliott, “Study of Model Superoleophobic Surfaces Fabricated with a Modified Bosch Etch Method”**.**

Acknowledgements

This research was funded by the Natural Sciences and Engineering Research Council (NSERC) of Canada.

I wish to thank my supervisors for their excellent instructional efforts and acknowledge their editing of this thesis.

I wish to acknowledge fellow students Andrew J. B. Milne and Guoping Fang, who provided comradery, instruction in the use of contact angle measurement equipment, valuable discussions, and collaboration on projects not presented in this thesis.

Finally, I wish to thank the staff at the University of Alberta's NanoFab for instruction in the fabrication tools needed to create the surfaces in this thesis.

Table of Contents

Table of Figures

Chapter 1 : Introduction

1.1 – Background

This thesis details our experimental studies on the contact angles of liquids with varying properties, most notably surface tension, on surfaces given micro- and nano-scale texturing via the use of microfabrication techniques originally pioneered by the semiconductor industry. The fabrication of these surfaces allowed for the investigation of questions surrounding how the geometry of micro-scale patterns affect contact angle and contact angle hysteresis. In performing the measurements and analyzing the data, new complexities already seen in the literature but not strongly commented upon became apparent. In order to address these complexities, a new conceptual framework for understanding contact angles was developed. In order to give context, a brief summary of the history and current state of affairs of the science of contact angles, contact angles on rough surfaces, and microfabrication as it relates to creating rough surfaces follows below.

The scientific study of contact angles begins with Young in 1805[1] wherein a force balance between the surface tensions, γ, of interfaces between solid, *S*, liquid, *L*, and vapor, *V* gives rise to the Young contact angle, θ_Y, at the line where all three phases meet, the so called contact line, and was described in words by Young in the form of Equation 1-1:

$$\gamma^{LV}\cos\theta_Y = \gamma^{SV} - \gamma^{SL} \qquad [1\text{-}1]$$

The Young contact angle represents the equilibrium contact angle on an ideal flat surface. As surfaces become non-ideal, *i.e.* are not chemically heterogeneous and/or have surface roughness, Equation 1-1 becomes less relevant but still important. The Young contact angle, also called the equilibrium or intrinsic contact angle, is an input value for the equations describing contact angle on rough surfaces,

and thus a change in the contact angle on a smooth surface will cause changes to the contact angle on rough surfaces made of the same material. The most typical cause of a change in contact angle is a change in the surface tension of the liquid, such as going from a high surface tension liquid like water (71.99 mN/m at Standard Ambient Temperature and Pressure (SATP))[2] to an intermediate liquid like ethylene glycol (47.99mN/m at SATP)[2] low surface tension alkane such as hexadecane (27.87 mN/m at SATP).[2]

In 1936 a paper by Wenzel[3] made a large step towards understanding contact angles and wetting on rough surfaces. Applying to surfaces where the liquid is in complete contact with the three-dimensional roughness, a situation called either homogenous wetting or the Wenzel state, the Wenzel equation gives the apparent macroscopic contact angle (or Wenzel contact angle, θ_W) as:

$$\cos\theta_W = r\cos\theta_Y \qquad [1\text{-}2]$$

where the Wenzel roughness, *r*, is the total three dimensional surface area in contact with the drop divided by the projected surface area bounded by the contact line of the drop. As can be seen, when the surface is smooth the Wenzel roughness becomes equal to 1 and the Wenzel equation gives the Young contact angle as its result. Also, as can be seen, Equation 1-2 serves to amplify the behavior of a liquid on the surfaces. Because there is a change in sign at $\cos(90°)$ and the cosine function cannot exceed a value of 1 or go below a value of –1, sufficiently large values of *r* should serve to cause drops with intrinsic contact angles below 90° to go to 0°, and those with contact angles above 90° to go to 180°.

Next in the development of the science of contact angles was the contribution of Cassie and Baxter[4] in 1944, who developed a method for predicting contact angles on heterogeneous surfaces. While generally applicable for any sort of chemical heterogeneity, in particular it has been used for surfaces

where the drop is partially in contact with the surface and partially in contact with air, a situation called either heterogeneous wetting or the Cassie state, in which case the form of the Cassie equation is:

$$\cos\theta_C = f_1 \cos\theta_Y - f_2 \qquad [1\text{-}3]$$

where f_1 is the ratio of solid-liquid contact area to the projected contact area of the drop bounded by the contact line, and f_2 is the ratio of liquid-air contact area to the projected contact area. Should f_2 go to 0 then Equation 1-3 reduces to Equation 1-2 and f_1 is the same as *r.* In the literature, particularly in cases with well-defined two-dimensional cross sectional geometry at the point of contact between the drop and the surface, it is assumed that $f_1 + f_2 = 1$ and the Cassie equation is reduced to:

$$\cos\theta_C = (\cos\theta_Y + 1)f - 1 \qquad [1\text{-}4]$$

where $f = f_1$ and is typically called the Cassie fraction. Because the Cassie state minimizes contact with the solid surface, if the intrinsic contact angle of the material is above 90° and the Wenzel roughness is large, the Cassie state becomes more favorable than the Wenzel state. For intrinsic contact angles around the sign change of 90°, the situation becomes more complex, as shall be explored.

The Wenzel and Cassie equations form the foundation of the study of contact angles and wetting on rough surfaces. However, they are only the foundation of understanding and there are many complexities they do not capture. Their biggest issue is that they only capture the equilibrium contact angles, which are not the contact angles typically observed in experiments. Experimentally what is observed are the advancing and receding contact angles, which are the highest and lowest possible contact angle configurations and they depend on the motion of the contact line. If the contact line is moving the drop to wet an area that has not yet been wetted by the drop, it is the advancing contact angle that is observed, while if the contact line is moving to unwet the drop from an already wetted area, it is the receding contact angle that is observed. While this definition includes both drops on level surfaces that are having their volumes increased and decreased, respectively, and drops on tilted

surfaces with the advancing and receding contact angles being at the leading and trailing edges, respectively, the two methods of measurement do not necessarily give analogous results to each other.[5] As shown by Johnson and Dettre[6] in 1964, Equations 1-2 and 1-3 are only valid for equilibrium contact angles and not for the advancing and receding contact angles.

The difference between the advancing and receding contact angles is called the contact angle hysteresis. The theoretical origins of this phenomenon has been extensively explored, with a significant examination beginning with Joanny and de Gennes[7] in 1984. They proposed contact angle hysteresis as arising from micro- or nano-scale local energy defects that would cause the contact line moving across them to pin on the defect, creating resistance to the motion of the contact line.

In terms of pinning, further developments to this way of thinking were made by Pomeau and Vannimenus[8] in 1985, who explored contact angle hysteresis as it might arise from weak heterogeneities, and by Raphaël and de Gennes[9] in 1989 when the single defect problem was more thoroughly explored. More recently Tadmor[10] explored the relationship between advancing, receding, and Young contact angles in 2004. These works are in depth theoretical explorations of thermodynamics and force, but to summarize, line pinning occurs when there is some sort of heterogeneity on a surface where it is more energetically favorable for the contact line to stay in one place locally rather than move with the rest of the contact line, leading to a distortion in the contact line until the force caused by surface tension becomes so great as to move the contact line off the heterogeneity.

By the 1990s, several developments brought significant renewed interest in the science of contact angles. While it would take some time to be available outside the semiconductor industry, the development of deep reactive ion etching procedures, such as the Bosch etch process first patented in 1994,[11] would eventually allow for surface scientists to begin fabricating surfaces with microscopic

feature sizes designed to have specific Wenzel roughness and Cassie fractions. Other methods that are available include self-assembly of aggregate nano-particles,[12] replication of existing natural structures via polymer moulding,[13] the chemical treatment of textile fibres,[14] the functionalization of carbon nanotubes,[15] spray cast coatings,[16] and anodization of metals such as aluminum,[17] to give a brief sample of the myriad processes. The biggest advantages that the reactive ion etching methods and photolithography have, for our purposes, is that they allow for very precise definition of geometric factors, allowing for values such as the Wenzel roughness and Cassie fraction to be pre-defined. Such methods are employed typically by first using a CAD program to develop a pattern that is then etched into a mask design via lasers or electron beams, depending on the resolution required. This mask then selectively protects a resin film from exposure to ultraviolet radiation, either breaking down or curing the film depending on chemistry such that the desired design is present on a silicon surface. This patterned film then protects parts of the silicon from various forms of chemical and plasma etching, transferring the pattern to the silicon. This allows for both production of precisely defined textured surfaces, and for easy replication of the same patterned surfaces, allowing for much more controlled experimental design and repetition of experiments.

In 1998 Wolansky and Marmur[18] discussed how on rough surfaces microscopic conformation to intrinsic contact angles can give rise to a different apparent macroscopic contact angle. This is an early demonstration of a focus within the literature upon attempting to discern through theory and experiment the microscopic effect of various changes to geometry and chemistry on contact angle. More recently Butt *et al.* have written numerous papers on the subject of the microscopic interactions that give rise to high contact angles.[19,20,21,22]

In 2000 Öner and McCarthy[23] used reactive ion etching to manufacture surfaces in silicon with various geometric arrangements and different chemical treatments to create chemical hydrophobicity to examine the effects of different length scales and geometric configurations upon contact angles, and

found that the length scales were more important for determining the stability of a drop in the Cassie state than for determining its actual contact angle.

In 2009 Reyssat and Quéré[24] used this sort of fabrication technique to produce surfaces with silicon pillars to examine whether or not the contact angle hysteresis formulation proposed by Joanny and de Gennes previously could be used on such surfaces, with each pillar representing a single defect. Their formulas showed good agreement for surfaces with a Cassie fraction below approximately f = 0.3 but divergence for the few surfaces they had that had higher Cassie fractions than that, indicating a breakdown in their initial assumptions, particularly that the pillars represented "dilute" defects that only contributed to contact angle hysteresis additively rather than having any interactions with each other.

Other similar studies on surfaces micropatterned with varying length scales have been done by Cansoy *et al.,*[25] Dorrer and Rühe,[26] and Priest *et al.,*[27] which have ambiguous results when taken as a whole. Some of the studies indicate that there is no dependency of contact angle upon feature size beyond the control of the Cassie fraction, while others do find changing contact angles with changing feature sizes even while maintaining the same Cassie fraction. The use of Equation 1-4 to generate predictions to which results can be compared is also uneven as well. This is exacerbated by the use of Equation 1-4 as if it were the original form of the Cassie equation rather than Equation 1-3, leading to general confusion in the field of study of contact angles on textured surfaces.[28]

One particular point that emerges from the examination of textured surfaces is that for surfaces with hydrophobic pillars,[25,26,27] the advancing contact angle will remain at a geometry-insensitive high contact angle while the receding contact angle will vary with varying Cassie fraction and other geometric factors. This behavior has been observed by Johnson and Dettre[6] and Morra *et al.*[29] on oxygen plasma treated poly(tetrafluoroethylene). The study by Priest *et al.*[27] studied not just hydrophobic pillars, but also pits and defined surface patches treated with hydrophobic or hydrophilic chemicals and surrounded by

chemicals with the opposite treatment, and it was found that whether the advancing or receding contact angle was more responsive depended on the type of surface used. This shows that not only is contact angle determined by more than just the equilibrium value predicted by equation 1-4, but that both the advancing and receding contact angles contain important information.

While they have received less attention in the literature, drops in the Wenzel state also show the importance of examining both the advancing and receding contact angles. A study by Dorrer and Rühe[30] in which they changed hydrophobic pillars to hydrophilic ones by changing the chemical coating on the pillars showed systems with large advancing contact angles and receding contact angles at 0°, when the contact angles predicted by Equation 1-2 were 0°. This phenomenon has also been seen by Zawodzinski *et al.*[31] while characterizing perfluorosulphonic acid membranes, where some of the membranes showed advancing contact angles in excess of 100° and receding contact angles of 0°. Work done by Forsberg *et al.*[32] on surfaces of SU-8 photoresist patterned with pillars showed advancing contact angles of 140° and receding contact angles of 0°. Even more extreme cases of this behavior have been observed by Balu *et al.*,[33] Peng *et al.*,[12] and Feng *et al.*,[34] with advancing and static contact angles exceeding 150° and the drops having either receding contact angles of 0° or no roll-off angle, the drops being capable of being suspended from an inverted surface.

Maintaining a drop in the Cassie state over the Wenzel state has been another area of intense research, with various discussions over the years by Marmur,[35] Li and Amirfazli[36] and Butt *et al.*,[19] to give a sample. This interest in the stability of the systems has to do with the numerous practical applications of superhydrophobic and superoleophobic surfaces.

Superhydrophobic surfaces are textured surfaces with water contact angles exceeding 150°, while superoleophobic surfaces are similar to superhydropobic surfaces but also applying to low surface tension oils as well. These are particularly useful for self-cleaning surfaces[37,38] and are of interest as anti-

icing surfaces[15,39,40] and for use in the print industry.[41] The largest issue for these surfaces, particularly superoleophobic surfaces, is maintaining the drops in the Cassie state rather than the Wenzel state as the Wenzel state is often thermodynamically more favorable.

One solution to create thermodynamically stable superoleophobic surfaces is the overhanging cap geometry widely explored by Tuteja *et al.*[42,43] Using differences in the chemistry of etching between silicon and silicon dioxide, surfaces where silicon dioxide caps sit on top of silicon pillars of lesser cross sectional diameter can be created. As explored by Fang and Amirfazli[44] the sharp edge created by the caps imposes an energy barrier that can help maintain a metastable Cassie state and thus allow for the creation of superoleophobic surfaces where they might not otherwise be favorable.

1.2 - Scope of the Thesis

This thesis seeks to explore three major questions in the area of surface science: i) how to reconcile contact angle equations being for intrinsic contact angles while observations are for advancing and receding contact angles; ii) how geometry affects the stability of the Cassie state over the Wenzel state, and; iii) how to combine together ideas about contact angle hysteresis with ideas about textured surfaces.

Chapter Two provides details of an experimental study examining the effects of feature size and Cassie fraction in combination on contact angle and contact angle hysteresis. It also introduces a new pinning force framework that provides an empirical way to describe the relationships between predicted equilibrium contact angles and observed advancing and receding contact angles for drops in the Cassie state, for water and ethylene glycol.

Chapter Three is an extension of the research done in Chapter Two, using hexadecane, a lower surface tension liquid, on the same surfaces. This extends the pinning force framework to include the Wenzel state and explores unexpected behaviors of surfaces with strong pinning in the Wenzel state, as well as

showing that hexadecane drops in the Cassie state have the same observed behaviors as water and ethylene glycol drops in the Cassie state.

Chapter Four features a successful attempt to produce a new procedure for creating surfaces featuring overhanging cap structures for superoleophobicity that allows for near arbitrary control of cross-sectional geometry and height of the pillars. Since water, ethylene glycol, and hexadecane were used as the test liquids, comparisons were also made between pillars with similar cross sectional geometry. This allowed for an examination on the effect of the overhanging caps on the stability of the Cassie state over the Wenzel state and the effect of the observed pinning forces.

Chapter 2: Modeling and Measurement of Contact Angle Hysteresis on Textured High-Contact-Angle Surfaces

2.1 – Introduction

Superhydrophobic and superoleophobic surfaces are a group of textured surfaces that show extreme repellency towards water and oils, respectively. They are a commercially and industrially significant class of materials for their uses in self-cleaning materials[45] and anti-icing surfaces.[46,47] Current fabrication techniques include spray coating,[48,49] polymer imprint moulding,[50] electrochemical etching of metals,[51] the hydrophobization of fibres in textiles,[52] plasma treatment of Teflon,[53] and photolithographic patterning of silicon and silicon dioxide.[54] Of these, perhaps the most important from a theoretical standpoint is photolithographic patterning as it allows for nearly arbitrary control of geometry, allowing for a deeper exploration of how geometric factors affect the wetting of such surfaces. In photolithographic patterning a two-dimensional pattern is transferred to a silicon surface and used to create an array of pillars via selective etching of the silicon.

Wetting, on either textured or smooth surfaces is described by contact angle (CA). On ideal smooth surfaces the equilibrium contact angle is the Young contact angle, θ_Y, defined by

$$\gamma^{LV}\cos\theta_Y = \gamma^{SV} - \gamma^{SL} \qquad [2\text{-}1]$$

where γ^{LV}, γ^{SV}, and γ^{SL} are the interfacial tensions of the liquid–vapour, solid–vapour, and solid–liquid interfaces, respectively. The Young equation can be thought of as an energy equation or a force balance and it should be recognized that these two ways of thinking are equivalent. The conditions for equilibrium from the thermodynamic perspective are found by minimizing free energy subject to constraints, including constant entropy, with interfacial tensions being introduced as surface excess internal energies per unit area.[55] The resulting conditions for equilibrium include thermal equilibrium,

chemical equilibrium and mechanical equilibrium. The mechanical equilibrium conditions, such as the Young equation, can also be found directly from force balances where surface tensions are conceptualized in terms of force per unit of contact line length. Throughout this chapter we use force-per-unit-length and energy-per-unit-area concepts interchangeably to better contextualize ideas.

Most surfaces possess contact angle hysteresis, which is the difference between the advancing (θ_{Adv}) and receding (θ_{Rec}) contact angles. When contact angles are measured from a drop with changing volume, the advancing contact angle is measured when the solid–drop contact area is increasing, and the receding contact angle is measured when the solid–drop contact area is decreasing. When measured from a tilted drop, the advancing contact angle is the angle measured from the surface of the leading edge of the drop just as it begins to slide and the receding contact angle is the angle of the trailing edge. While these two methods of determining the advancing and receding contact angles have been treated as synonymous in the past, more recent research by Pierce *et al.*[56] suggests that this is not necessarily true.

One method of approximating the equilibrium Young contact angle on surfaces with contact angle hysteresis is the method of cosine averaging,[57]

$$\cos\theta_Y = \frac{(\cos\theta_{Adv} + \cos\theta_{Rec})}{2} \qquad [2\text{-}2]$$

This method has limitations, and for some surfaces an unequal weighting between advancing and receding contact angles produces a better fit,[58] but for many smooth surfaces with hysteresis Equation 2-2 serves as a good method for finding the equilibrium contact angle.[58] Also in the literature[59,60] one can find a simple averaging of θ_{Adv} and θ_{Rec} to estimate θ_Y. For smooth surfaces, this study will use Equation 2-2, however. These averaging methods are also empirical relations, obtained from experiment, and not from any theoretical backing.

There are two primary wetting modes on textured surfaces: penetrated wetting or the Wenzel state,[61] and non-penetrated wetting or the Cassie state.[62] For surfaces with roughness and penetrated wetting, the Wenzel equation[61] gives the apparent macroscopic contact angle, θ_W, as

$$\cos\theta_W = r\cos\theta_Y \qquad [2\text{-}3]$$

where *r* is the Wenzel roughness factor, defined as the actual area of solid in contact with the liquid divided by the projected contact area of the drop bounded by the contact line.

For surfaces with roughness and non-penetrated wetting, the Cassie equation[62] gives the apparent macroscopic contact angle, θ_C, as

$$\cos\theta_C = f_1\cos\theta_Y - f_2 \qquad [2\text{-}4]$$

where f_1 is the ratio of the solid–liquid contact area to the projected area of the drop bounded by the contact line, and f_2 is the ratio of the air–liquid contact area under the drop to the projected contact area of the drop bounded by the contact line. In general,[63] for non-planar or partially engulfed pillars $f_1 + f_2 \geq 1$, but for most photolithographically defined surfaces with flat topped pillars it can be assumed[63] that $f_1 + f_2 = 1$, which yields the simplified Cassie equation

$$\cos\theta_C = (\cos\theta_Y + 1)f - 1 \qquad [2\text{-}5]$$

where $f = f_1$ and is called the Cassie fraction, defined in the cases of interest (see Section 3) here as

$$f = \frac{\#\ of\ pillars\ in\ a\ unit\ cell \times cross\ sectional\ area\ of\ 1\ pillar}{area\ of\ unit\ cell} \qquad [2\text{-}6]$$

It is to be noted that, like the Young equation, the Cassie and Wenzel equations are equilibrium equations, so they need to be altered in some way to deal with the complexities of advancing and receding contact angles. The use of advancing and receding contact angles directly within equilibrium equations has been seen in the literature all the way back to the original paper by Cassie and Baxter[62] in 1944 but was shown to be incorrect as early as 1964 (see Johnson and Dettre[64]) and there has been

confusion in applicability and use within the literature ever since. It is a primary goal of this work to provide a general framework to move forward.

The effects of patterned geometry on contact angle and contact angle hysteresis have been previously studied, but a full exploration of geometric effects has yet to be done. Öner and McCarthy[65] performed a series of experiments with arrays of pillars of square and circular cross-sections with varying sizes and spacing of the pillars. They found no significant variation in contact angle with changing pillar size, but they did not vary the Cassie fraction, keeping it constant over all of the surfaces. They also did not make any comparison to the equilibrium contact angles predicted by theory. Cansoy *et al.*[66] performed experiments with varying pillar sizes, spacing, and Cassie fractions and made comparisons with contact angles predicted by Equation 2-5, but there was only one data set where size and spacing of the pillars were varied to produce similar Cassie fractions, with all other surfaces having only one combination of Cassie fraction and pillar size examined.

Perhaps most significantly, Dorrer and Rühe[67] performed experiments on patterned surfaces where the spacing and sizes of the pillars were varied, but the Cassie fractions were also kept constant for some of the cases studied. Their study showed two important features that are useful for further discussion. The first is that the advancing contact angle was mostly insensitive to the Cassie fraction, a surprising result considering Equation 2-5. Secondly, the receding contact angle did change with changing Cassie fraction, a behavior seen in other literature such as that of Dettre and Johnson[64] and Morra *et al.*[53] Also seen was that the larger the pillar size and pillar spacing, while maintaining the same Cassie fraction, the lower the receding contact angle. No attempt to compare these values with theoretical models such as Equation 2-3, Equation 2-4, or Equation 2-5 was made,[67] but a subsequent paper by Dorrer and Rühe[68] examined contact angles on the same surfaces but altered their surface chemistry to make them fully wetting. In that study they found that for high roughness surfaces with a hydrophilic coating there was

a deviation from values predicted by Equation 2-3 for advancing contact angles while the receding contact angles followed the predicted behavior of complete wetting.

Another work by Priest *et al.*[27] studied square pillars, holes, and patches of altered chemistry that were hydrophilic or hydrophobic, all of which had square geometry with dimensions 20 μm across, and Cassie fractions varying from 0 to 0.80. They found that the form of the surface and whether a drop was advancing or receding influenced whether it agreed or not with the predictions of the Cassie equation. For example, with chemically hydrophobic patches they found that when the drop was in the advancing state its measured contact angle disagreed with the predictions of the Cassie equation but that in the receding state its measured contact angle agreed with the Cassie equation. In particular for their hydrophobic pillars, they found that advancing contact angles did not agree with the predictions of the Cassie equation, and in fact remained near constant, while the receding values only qualitatively agreed with the predictions of the Cassie equation.

Considering that for these prior studies there is a marked trend towards the advancing contact angle being invariant and the receding contact angle changing with changing pillar geometries, this means that the contact angle hysteresis will change with changing geometry and thus a better understanding of contact angle hysteresis on textured surfaces is needed.

For surfaces with contact angle hysteresis, Joanny and de Gennes[69] proposed a theoretical framework that looks at contact angle hysteresis as arising from energy defects on an ideally smooth and homogeneous surface. They began by proposing that an energy defect was a patch of arbitrary dimension on a surface that had a different surface energy from the surrounding material, leading to a deformation of the contact line. For a macroscopic system, they proposed for a drop sitting upon an array of such energy defects, each with an individual defect energy W_d, that contact angle hysteresis is explained by Equation 2-7.

$$\gamma^{LV}(\cos\theta_{Rec} - \cos\theta_{Adv}) = nW_d \quad [2\text{-}7]$$

where

$$n = \frac{\#\ of\ defects}{area} \quad [2\text{-}8]$$

One of the assumptions of Joanny and de Gennes was that the defects were in a dilute regime, *i.e*. that defects are sufficiently far apart that the energy contributions from each defect are simply additive and that defects do not influence one another. While the argument was primarily about chemical defects, the discussion was generalized by Joanny and de Gennes to include surface roughness defects and included a brief discussion about apparent contact angles on surfaces with roughness determined by a continuous topographical function, $u(x, y)$, suggesting that apparent contact angles would be given by

$$\gamma^{LV}\cos\theta = \gamma^{SV} - \gamma^{SL} + h \quad [2\text{-}9]$$

where *h* was defined as

$$-h(x, y) = \cos\theta_Y \frac{du}{dy} \quad [2\text{-}10]$$

We will not be building directly from the work of Joanny and de Gennes. It is included here to give a complete picture of the previous literature. Rather, we are taking a macroscopic viewpoint in which a complex surface gives rise to additional forces that alter the advancing and receding contact angles from the expected equilibrium contact angles. The aggregate effect of these forces will be captured from experiment in our work. Relating the details of microscopic energy defects to macroscopic behavior is beyond the scope of this work, although Reyssat & Quéré[24] have examined contact angle hysteresis on micropillar arrays assuming each pillar represents a single strong defect as envisioned by Joanny and de Gennes. They found good agreement when the system was dilute, but at Cassie fractions above 0.3 their experimental results started to diverge from their theoretical model, and the majority of their

experimental data points were at Cassie fractions below 0.2. The study, here, however expands the range for *f* as a majority of our experimental data is at Cassie fractions above 0.3.

Although these previous works made important contributions, there is still ambiguity as to whether or not changing the size of surface features while keeping the Cassie fraction constant has an effect on contact angle, and there is currently no way to predict, theoretically or empirically, the contact angle hysteresis of a textured surface based on geometric factors.

In the study reported herein, we fabricated a set of surfaces with a range of pillar geometries that result in both surfaces with a range of Cassie fractions, and surfaces with different pillar diameters and spacing combinations but the same Cassie fraction. We then measured the advancing and receding contact angles of both water and ethylene glycol on these fabricated surfaces. The first objective of this work was to determine if varying pillar diameter while keeping Cassie fraction the same produces significantly different advancing or receding contact angles. The second objective was to develop a new theoretical framework for understanding the advancing and receding contact angles that were measured.

2.2 - Governing Equations

2.2.1 Pinning Force Framework for Smooth Surfaces

Following a similar line of thinking to Joanny and de Gennes, we propose the inclusion of an extra surface energy per unit area, a "pinning force" per unit length, F_P, to explain the difference between equilibrium and non-equilibrium states. Unlike in Equation 2-9, we shall not make the assumption that F_P stems from variations in topography but allow it to include both topography and chemistry in totality. The proposed form for the receding contact angle on a smooth surface is thus

$$\gamma^{LV}\cos\theta_{Rec} = \gamma^{SV} - \gamma^{SL} + F_P \qquad [2\text{-}11]$$

Inserting the definition of the Young contact angle from Equation 2-1 into Equation 2-11 and rearranging, yields:

$$\cos\theta_{Rec} = \cos\theta_Y + \frac{F_P}{\gamma^{LV}} \qquad [2\text{-}12]$$

For the smooth surface making the assumption that the non-dimensional pinning force, $\frac{F_P}{\gamma^{LV}}$, is equal and opposite when the contact line is advancing rather than receding gives

$$\cos\theta_{Adv} = \cos\theta_Y - \frac{F_P}{\gamma^{LV}} \qquad [2\text{-}13]$$

Adding Equations 2-12 and 2-13 together yields

$$\cos\theta_{Adv} + \cos\theta_{Rec} = 2\cos\theta_Y \qquad [2\text{-}14]$$

giving theoretical justification for the cosine averaging formula in Equation 2-2 for smooth surfaces. Subtracting 2-13 from 2-12 gives

$$\gamma^{LV}(\cos\theta_{Rec} - \cos\theta_{Adv}) = 2F_P \qquad [2\text{-}15]$$

which is similar in form to the equation proposed by Joanny and de Gennes,[69] Equation 2-7. We have noted above that the concepts of force per unit length ($2F_P$) or energy per unit area (nW_D) are interchangeable in mechanical equilibrium equations, so in that way the two equations appear similar. However, in contrast to the thinking of Joanny and de Gennes who considered specific, dilute defects, since for a realistic surface the pinning force can be affected by chemical heterogeneity, roughness, and interactions between defects, the purpose of this work is to include pinning forces in a more global framework and to obtain the pinning forces from measurements. While we called our term a "pinning" force, it need not arise from actual pinning. As has been shown in the past by Wolansky and Marmur,[18] apparent contact angle changes on rough surfaces can be shown to arise from a local conformation to intrinsic contact angle. As such, it is important to understand that the term $\frac{F_P}{\gamma^{LV}}$, which is called the

pinning force here, is an empirically determined, macroscopic descriptor of all microscopic interactions that give rise to deviations between the equilibrium contact angle and the advancing and receding contact angles.

Now two important limits that this formulation imposes emerge, owing to the fact that contact angles cannot be greater than 180° or less than 0°

$$\cos\theta_Y - \frac{F_P}{\gamma^{LV}} \geq -1 \qquad [2\text{-}16]$$

$$\cos\theta_Y + \frac{F_P}{\gamma^{LV}} \leq 1 \qquad [2\text{-}17]$$

2.2.2 Proposed Pinning Force Framework for Non-Penetrated (Cassie) Wetting Rough Surfaces

Here we generalize the pinning force framework from a smooth surface to a rough surface in the case of Cassie wetting by replacing the Young equilibrium contact angle in Equation 2-12 with the Cassie contact angle. Thus, it is proposed that for receding contact angles on rough surfaces, $\theta_{Rec,rough}$, one can write:

$$\cos\theta_{Rec,rough} = \cos\theta_C + \frac{F_{P_{Rec,rough}}}{\gamma^{LV}} \qquad [2\text{-}18]$$

where θ_C is, as in Equation 2-5, the predicted Cassie contact angle, and $\frac{F_{P_{Rec,rough}}}{\gamma^{LV}}$ is the non-dimensional pinning force specifically upon the rough surface when a drop is in the Cassie (*i.e.* non-penetrated) state. For rough surfaces we relax the assumption that the pinning force is equal for advancing and receding contact angles due to literature's and our experimental evidence, seen below. Thus, for the advancing contact angles $\theta_{Adv,rough}$, we propose

$$\cos\theta_{Adv,rough} = \cos\theta_C - \frac{F_{P_{Adv,rough}}}{\gamma^{LV}} \qquad [2\text{-}19]$$

which has its own non-dimensional pinning force value $\frac{F_{P_{Adv,rough}}}{\gamma^{LV}}$. Again noting that the advancing contact angle cannot be larger than 180°, Equation 2-19 implies:

$$\cos\theta_C - \frac{F_{P_{Adv,rough}}}{\gamma^{LV}} \geq -1 \qquad [2\text{-}20]$$

With these equations and limits it thus becomes possible to begin analysis of the behavior of rough surfaces with contact angle hysteresis in an experimental setting to examine the validity of this framework.

2.3 - Materials and Methods

To minimize the effects of asymmetrical expansion across the surface, the geometry used in this study consisted of circles in a hexagonal packing arrangement, the unit cell of which is seen in Figure 2-1, where *d* is the pillar cross-sectional diameter; *s* is the edge-to-edge separation; *x* is the centre-to-centre separation (equal to *d + s*); and *f* is the Cassie fraction.

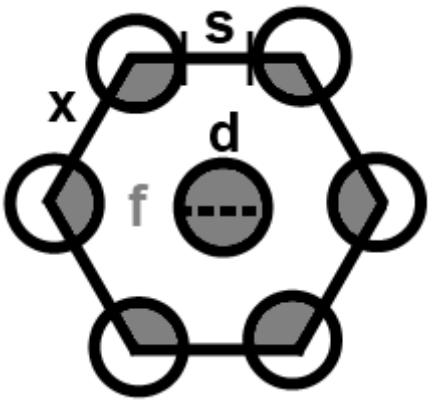

Figure 2-1 – Top-view diagram of the packing geometry of the pillars and relevant dimensions. Solid straight lines define the boundaries of the unit cell

For this system of circular pillars in a hexagonal packing arrangement *f* can be calculated as

$$f = \frac{\pi d^2}{\sqrt{12}(d+s)^2} \qquad [2\text{-}21]$$

To evaluate a broad range of pillar sizes and Cassie fractions and to examine for any interaction between the two parameters, 17 different surfaces, “Cases”, were fabricated. These Cases were divided into three different series of near constant Cassie fraction spread out over five different pillar diameters,

with two additional inter-series Cases that have common diameters but different Cassie fractions. Also included in the fabrication were several flat sections that were protected from etching for the purposes of providing smooth surfaces on which to measure intrinsic contact angle data.

Fabrication began with the cleaning of organic residue from the surface of a fresh silicon wafer via immersion in a 3:1 ratio solution of 96% sulfuric acid and 30% hydrogen peroxide. Once all organic residue was removed the silicon wafer had a layer of hexamethyldisilazane (HDMS) applied to allow better cohesion between the wafer and photoresist. A layer of HPR 504 photoresist from Fujifilm approximately 1.25 μm thick was applied via spin coating and then soft baked on a hot plate at 115 °C for 90 seconds before being allowed to sit for 15 minutes to reabsorb moisture from the surrounding air. Once the photoresist stabilized it was patterned with UV light and a mask aligner from ABM Inc., and the exposed photoresist dissolved via Microposit 354 developer. The wafer was then etched using the Bosch etching process[70] using a Surface Technology Systems Advance Silicon Etcher High Resonance Magnet (STS ASE HRM). In the Bosch etch, sulphur hexafluoride (SF_6) and octafluorocyclobutane (C_4F_8) plasmas alternate, with the SF_6 serving as an isotropic silicon etchant while the C_4F_8 deposits and forms a passivation layer on the sidewalls of the substrate being etched, preventing etching except in the direction of plasma bombardment, creating vertical, scalloped sidewalls. This process was used to create pillars 30 μm tall, with scallops on the sidewalls on the order of < 200 nm in diameter, which were deemed to be small enough that they would not significantly contribute to the behaviour of the fluids on the surface, especially since in our experimental Cases and theoretical formulation of the liquid behaviour the liquid sits on the tops of the pillars and thus does not interact with the scallops. Once the etching was finished the photoresist layer was removed with sequential washes of acetone, isopropyl alcohol, and deionised water, and then had a final removal of remaining process polymer contaminants via oxygen plasma in a Branson 3000 barrel etcher for 10 minutes.

The wafers were then examined in a LEO 1430 scanning electron microscope (SEM) from both a top down angle (0°) and an oblique angle (75°) so that the surface area of the tops of the pillars and the sidewall geometries could be examined, respectively. Top down SEM images of Case 1 through Case 5 can be seen in Figure 2-2-A through Figure 2-2-E, respectively, showing the increasing size of pillars while maintaining the same Cassie fraction. One of the oblique images can be seen in Figure 2-2-F, which shows pillars 40 µm in diameter with 6 µm edge-to-edge separation.

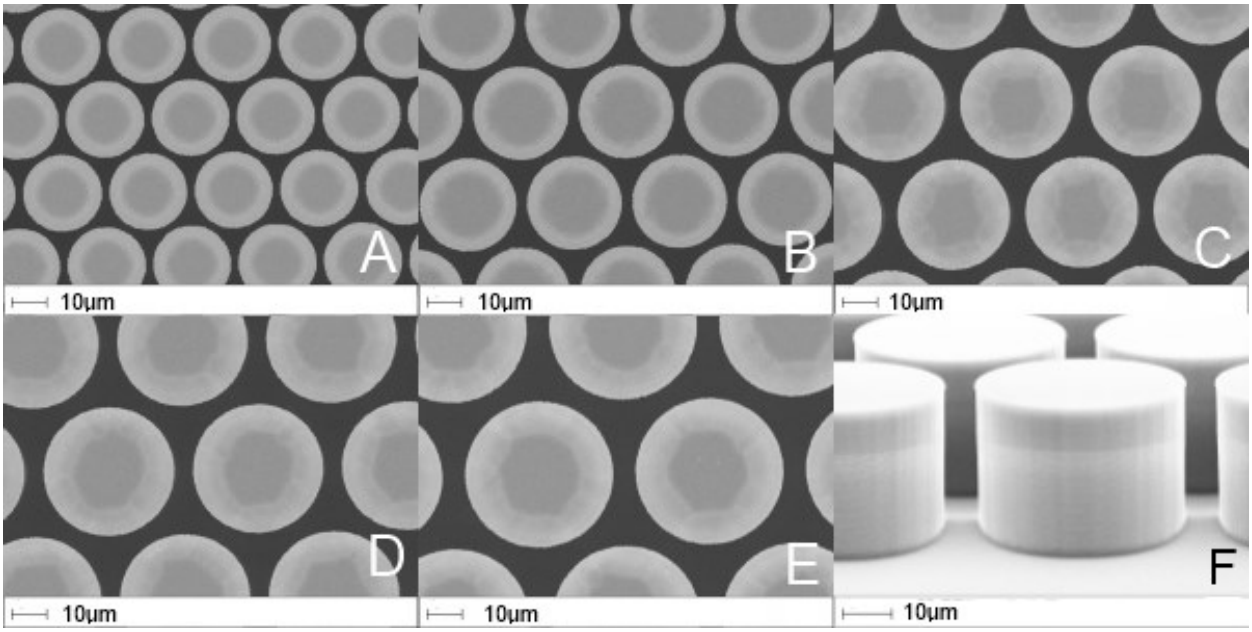

Figure 2-2 – SEM images of micropillars viewed at 3500X magnification for all images. A through E show Case 1 through Case 5, respectively, at a 0° angle and the increase in pillar diameter from 20 µm to 40 µm while maintaining the same Cassie fraction of approximately 0.69. For exact Cassie fraction values see Table 2-1. F shows the 40 µm pillars, the same as in E, at a 75° angle

After initial examination by SEM, it was noted that the actual pillar diameters for all Cases were approximately 2 µm larger than designed for, prompting use of an isotropic silicon etching using a Trion RIE Phantom system etch machine and a second measuring of the pillar dimensions. The final dimensions are presented in Table 2-1.

Table 2-1 – The measured parameter values for each of the fabricated Cases after final etch in the Trion RIE

Case	Diameter (μm)	Edge-to-edge separation (μm)	Cassie Fraction
Case 1	22.4±0.3	2.0±0.3	0.762±0.002
Case 2	25.8±0.7	2.9±0.5	0.732±0.004
Case 3	30.8±0.2	4.7±0.3	0.684±0.001
Case 4	35.7±0.7	5.3±0.3	0.689±0.003
Case 5	42.3±0.3	6.1±0.4	0.692±0.001
Case 6	26.0±0.6	7.1±0.6	0.560±0.005
Case 7	21.2±0.3	12.0±0.5	0.371±0.004
Case 8	25.7±0.3	15.5±0.3	0.353±0.003
Case 9	30.5±0.4	18.7±0.5	0.349±0.004
Case 10	34.7±0.8	22.8±0.5	0.331±0.006
Case 11	40.0±0.3	26.0±0.3	0.333±0.002
Case 12	25.0±0.2	32.7±0.2	0.170±0.001
Case 13	20.9±0.4	45.5±0.5	0.090±0.002
Case 14	25.6±0.2	56.9±0.3	0.087±0.001
Case 15	30.2±0.2	68.9±0.2	0.084±0.001
Case 16	35.2±0.2	80.54±0.3	0.084±0.001
Case 17	40.0±0.4	91.7±0.2	0.084±0.001

Next, the surfaces were treated to make them chemically hydrophobic. To produce an even, hydrophobic chemical coating the wafer was exposed to vapour phase trichloro(1H,1H,2H,2H-perfluorooctyl)silane from Sigma-Aldrich while under house vacuum pressure conditions in a bell jar.

Once made hydrophobic, the advancing and receding contact angles of water and ethylene glycol were measured. The contact angle on each Case was measured a minimum of three times using a custom optical goniometer that captured images of the drops so that they could be analyzed using ImageJ[71] and the Drop Snake profile tracing plugin.[72,73] The goniometer was mounted on an optical table to minimize external vibration, and any other effects of minor sources of vibration would be accounted for in the experimental error of measurement. All measurements were taken from the same orientation so that any dependence of contact angle on direction of motion across the surface (although anticipated to be minor due to the geometry of pillars chosen) would not confound the measurements. For each

measurement, a drop was grown with an initial volume of 25 µL on the surfaces so as to ensure proper formation and that the drop did not risk moving off the edge of a particular Case. Once satisfied that the drop was appropriately formed, its volume was increased to 75 µL at a rate of 0.5 µL/s while taking images. After reaching a volume of 75 µL, the volume was then decreased at a rate of 0.5 µL/s to a volume of 10 µL. This methodology ensured that the drops always remained in the advancing or receding state, with these states being determined by constantly checking that the radius of the contact line was moving before accepting a measurement as valid. Figure 2-3 shows an example of these drops in the advancing and receding states. After removal of the drops, no fluid was observed to have remained within the roughness, demonstrating that the drops remained in the Cassie state the entire time.

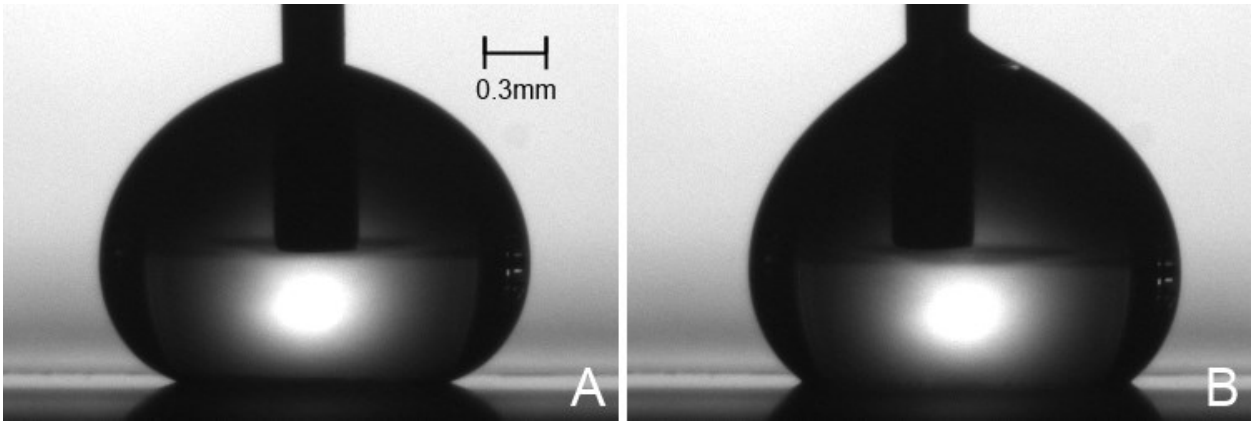

Figure 2-3 – Images of a water drop on Case 5. A shows the advancing state and B shows the receding state

One issue is that when contact angle approaches 180° drawing a proper tangent line becomes difficult[74] and it has been determined by Extrand and Moon[75] that for drops of microliter sizes gravitational flattening can further obfuscate high contact angles, introducing uncertainties in measurement on the order of 10°. However, the recommended maximum size given by Extrand and Moon[75] of hundreds of picolitres to avoid the effects of gravitational flattening is impractical for our purposes since such droplet sizes: cannot capture the macroscale effects of our roughness, are not representative of droplet

sizes in many applications, and would not be amenable to the standard methods of examination such as ours, which generally use drops ranging from in volume from 5 µL[66] to 200 µL.[59]

2.4 – Results and Discussion

2.4.1 Water Results

Table 2-2 shows the raw data for water, organized by Case.

Table 2-2 – Advancing and receding contact angles for water

	Advancing Contact Angle (°)	Receding Contact Angle (°)
Case 1	168±3	99±1
Case 2	169±1	102±1
Case 3	167±5	104.1±0.5
Case 4	171±1	102±1
Case 5	171±1	102±1
Case 6	171±1	109±1
Case 7	171±1	122±1
Case 8	171±1	119±1
Case 9	171±1	121±1
Case 10	170±1	121±1
Case 11	172±1	120±1
Case 12	170±2	132±1
Case 13	169±2	141±1
Case 14	170±1	140±1
Case 15	168±2	139±1
Case 16	169±1	141±1
Case 17	172±4	140±1
Smooth	113±1	91±2

Figure 2-4 shows the raw data for advancing and receding contact angles for water versus the pillar diameter. The inter-series Cases 6 and 12 were excluded as they cannot be used to investigate the independence of receding contact angle from pillar diameter, and would thus only clutter the figure. Through statistical analysis via ANOVA it can be shown that within series (*i.e*. for Cases with the same

Cassie fraction) the pillar diameter has no influence on advancing or receding contact angles ($p >> 0.05$) for all series with pillar diameters between 20 µm and 40 µm.

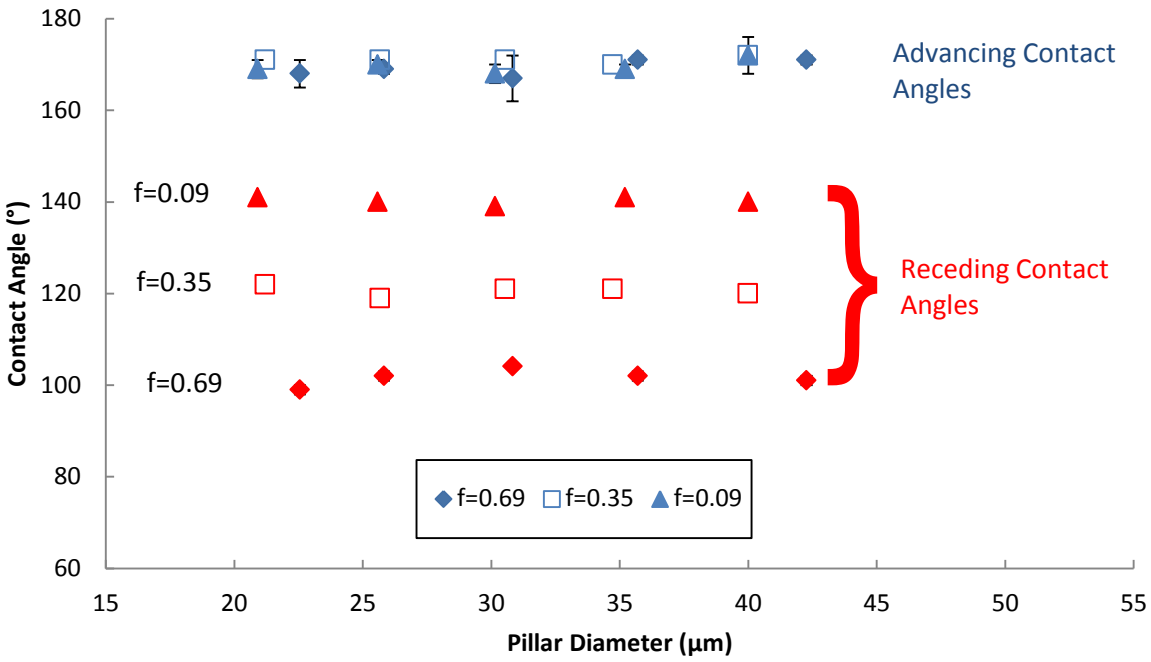

Figure 2-4 – Experimental advancing and receding contact angles for water plotted against pillar diameter, with Cassie fraction kept constant within each set of Cases. Error bars are either within the symbols or are shown

Figure 2-5 shows the raw data for all Cases for measured advancing and receding contact angles for water plotted against Cassie fraction, with the measurements from the smooth surface reported at $f = 1$ with cross symbols. The Young contact angle is determined by Equation 2-2, and then input into Equation 2-5 to obtain the predicted equilibrium Cassie contact angle (solid line in Figure 2-5). The other two lines in Figure 2-5 were drawn by using experimental advancing and receding contact angles from the smooth surface directly in the Cassie equation, Equation 2-5, in place of the Young contact angle, a method that has been used in literature in the past[27,76,77] but has no theoretical support. As expected these *ad hoc* predictions do not provide a better framework for understanding both advancing and receding contact angles.

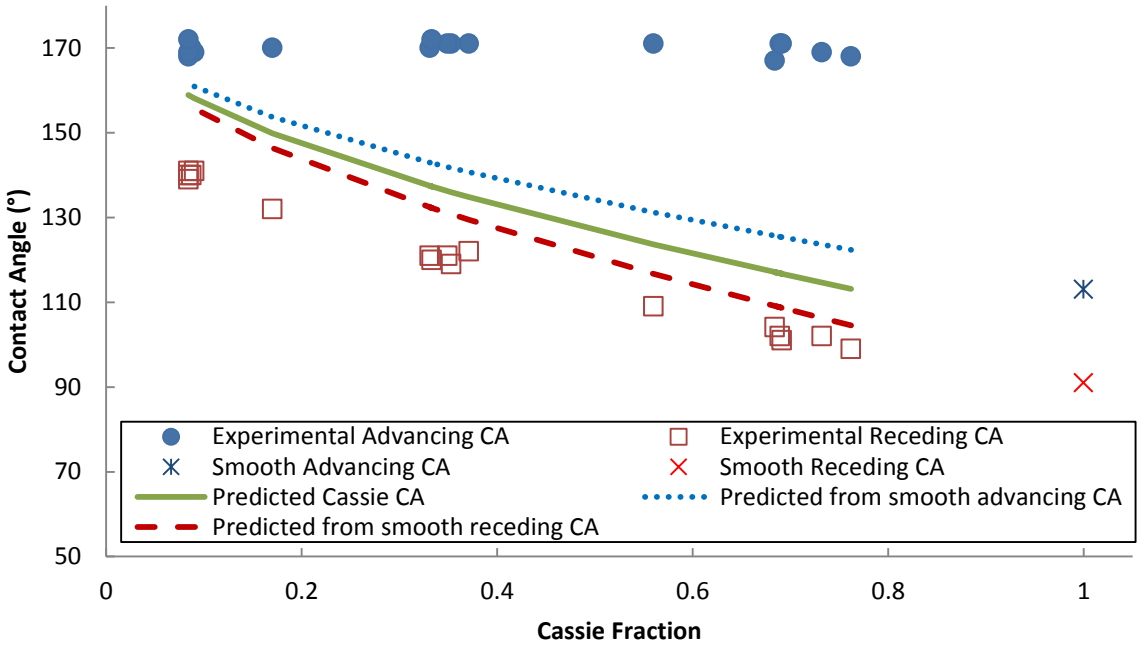

Figure 2-5 - Experimental advancing and receding contact angles for water compared with three predictions. Cassie contact angle is predicted with Equation 5, while the dashed line predictions are made by using the measured smooth advancing or receding contact angles directly in Equation 5 in place of the Young contact angle

The non-dimensional pinning force observed from the receding contact angles can be calculated from a rearrangement of Equation 2-18:

$$\frac{F_{P_{Rec,rough}}}{\gamma^{LV}} = \cos\theta_{Rec_{Exp}} - \cos\theta_C \qquad [2\text{-}22]$$

Equation 2-19 can be similarly rearranged to calculate the advancing pinning forces:

$$\frac{F_{P_{Adv,rough}}}{\gamma^{LV}} = \cos\theta_C - \cos\theta_{Adv_{Exp}} \qquad [2\text{-}23]$$

Applying Equation 2-22 to all the measured receding contact angles and Equation 2-23 to all the measured advancing contact angles generates the values seen in Figure 2-6

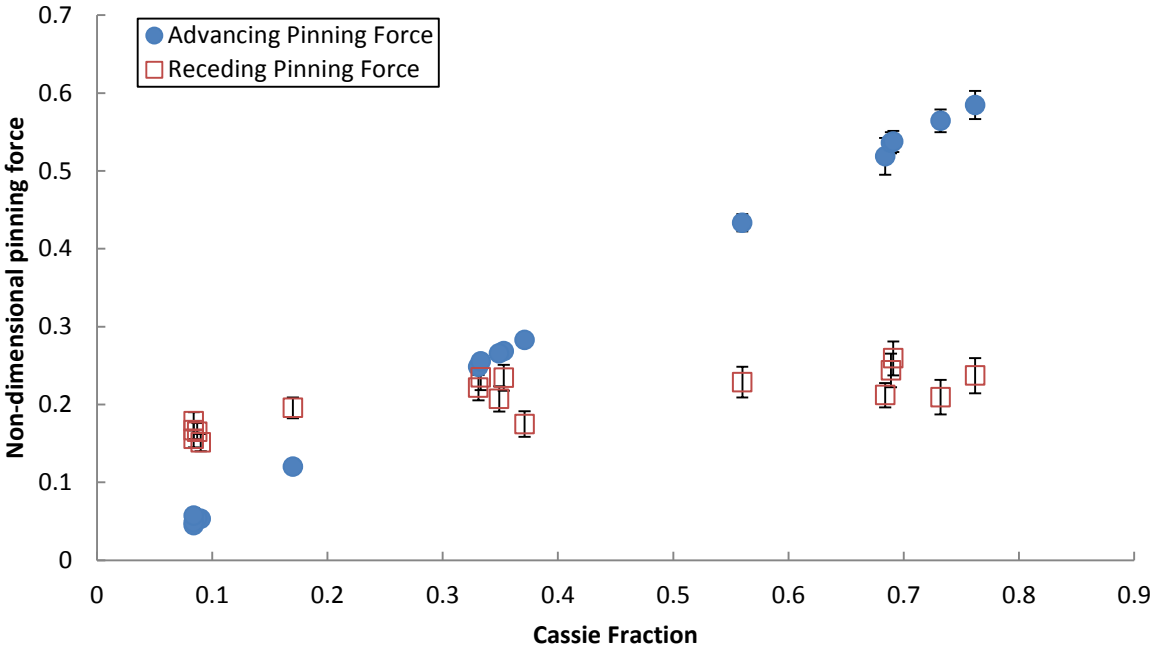

Figure 2-6 - Comparison between the calculated advancing non-dimensional pinning forces ($\frac{F_{P_{Adv,rough}}}{\gamma^{LV}}$) and the receding non-dimensional pinning forces ($\frac{F_{P_{Rec,rough}}}{\gamma^{LV}}$) for water. Error bars are either within the symbol size or shown

Figure 2-6 demonstrates the existence of a nearly constant observed pinning force for the receding contact angles and a steadily changing observed pinning force for the advancing contact angles. It also shows that for Cassie fractions greater than f = 0.33, the observed non-dimensional pinning force during advancing is greater than the observed pinning force during receding. In particular, it is clearly shown that $\frac{F_{P_{Adv,rough}}}{\gamma^{LV}} \neq \frac{F_{P_{Rec,rough}}}{\gamma^{LV}}$. For some of the Cases, specifically those with a Cassie fraction less than 0.2, if the limit seen in Equation 2-20 has been reached it would be impossible to detect the full strength of the pinning force, and it is possible that $\frac{F_{P_{Adv,rough}}}{\gamma^{LV}} = \frac{F_{P_{Rec,rough}}}{\gamma^{LV}}$. However, for the rest of the Cases this is not the situation and thus the discrepancy cannot be explained by use of the limit described by Equation 2-20.

There are important consequences resulting from advancing and receding pinning forces not being equal. Of particular importance is the fact that cosine averaging cannot be used for these rough

surfaces, since as shown in the development of Equation 2-14 for smooth surfaces, equality of advancing and receding non-dimensional pinning forces is a requirement for cosine averaging to be valid. The inequality of advancing and receding non-dimensional pinning forces on rough surfaces is consistent with the observation that cosine averaging that gives equal weight to advancing and receding contact angles is known to work only for macroscopically homogenous surfaces.[58]

The average value of $\frac{F_{P_{Rec}}}{\gamma^{LV}} = 0.20 \pm 0.03$ can be substituted into Equation 2-18 less the uncertainty, resulting in an empirical equation for the Cases studied here

$$\cos\theta_{C_{Rec,rough,water}} = \cos\theta_C + 0.2 \qquad [2\text{-}24]$$

or alternatively

$$\cos\theta_{C_{Rec,rough,water}} = (\cos\theta_Y + 1)f - 0.8 \qquad [2\text{-}25]$$

A linear regression of the advancing pinning forces gives

$$\frac{F_{P_{Adv,rough}}}{\gamma^{LV}} = 0.7933f - 0.0145 \qquad [2\text{-}26]$$

which can be substituted into Equation 2-19 to produce the empirical equation

$$\cos\theta_{Adv,rough} = (\cos\theta_Y + 1)f - (0.7933f - 0.0145) - 1 \qquad [2\text{-}27]$$

In Figure 2-7, the cosines of the experimentally measured receding contact angles are shown together with Equation 2-25 and the cosines of the experimentally measured contact angles are shown together with Equation 2-27, with all plotted against Cassie fraction.

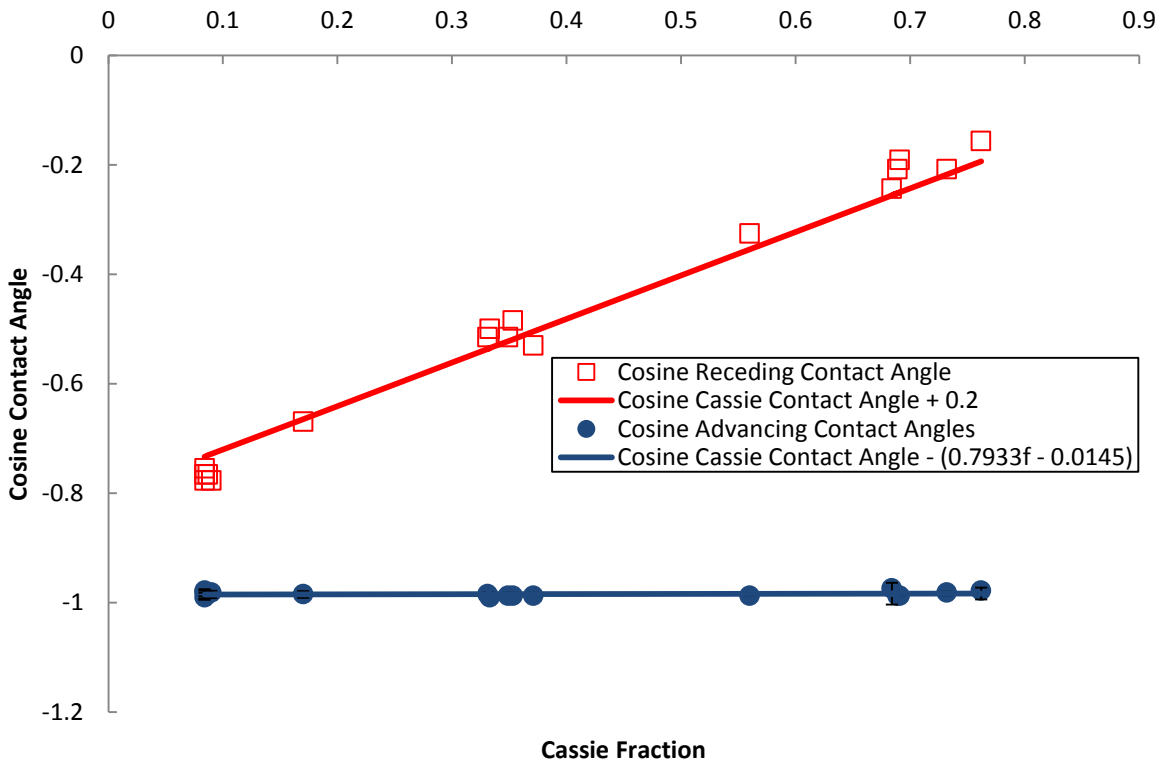

Figure 2-7 – Cosines of experimental contact angles compared with their empirical predictive equations and plotted against Cassie fraction for water

Restricting interpolation from Equation 2-25 and 2-27 to only the same geometric or chemical configurations as were used in this study, Figure 2-7 provides evidence that the advancing and receding contact angle can be empirically captured with a high degree of confidence across a broad range of Cassie fractions.

2.4.2 Ethylene Glycol Results

Table 2-3 shows the raw data for ethylene glycol, organized by Case.

Table 2-3 – Advancing and receding contact angles for ethylene glycol. *Cases 9 and 10 were damaged during testing did not give consistent results after and so were excluded from consideration

	Advancing Contact Angle (°)	Receding Contact Angle (°)
Case 1	136±4	86±1
Case 2	146±4	88±1
Case 3	152±3	91±3
Case 4	140±2	92±1
Case 5	154±2	87±4
Case 6	161±1	99±2
Case 7	162±5	111±1
Case 8	157±2	112±1
Case 9	*	*
Case 10	*	*
Case 11	170±3	111±1
Case 12	169±3	124±1
Case 13	171±1	133±2
Case 14	170±4	131±1
Case 15	171±3	132±2
Case 16	171±1	133±2
Case 17	170±5	133±2
Smooth	90±1	76±1

Figure 2-8 shows the raw data for advancing and receding contact angles for ethylene glycol, excluding the inter-series Cases 6 and 12. For the f=0.69 Series when performing ANOVA for advancing contact angles of all Cases there is a statistical difference between Cases with different pillar diameters ($p < 0.05$) but Cases 1 and 2 have Cassie fractions considerably larger than Cases 3 to 5 (f = 0.76 and 0.73 compared to f = 0.69). When considering Cases 1 and 2 and Cases 3 to 5 as being separate series both show no statistical dependence upon pillar diameter ($p > 0.05$) for the range tested. For all Cases in the f=0.69 series the receding contact angles are independent of the pillar diameter ($p > 0.05$). The f=0.35 series shows a statistical dependence for advancing and receding contact upon pillar diameter, but the magnitudes of the dependence of 0.2°/µm and 0.05°/µm are less than the sensitivity of the instruments

over the range tested and thus insignificant in comparison to the dependence upon Cassie fraction. For the f=0.09 series both the advancing and receding contact angles show no statistical dependence upon the pillar diameter ($p >> 0.05$). Based on this analysis for these surfaces, we conclude that ethylene glycol advancing and receding contact angles show no dependence upon pillar diameter at a fixed Cassie fraction.

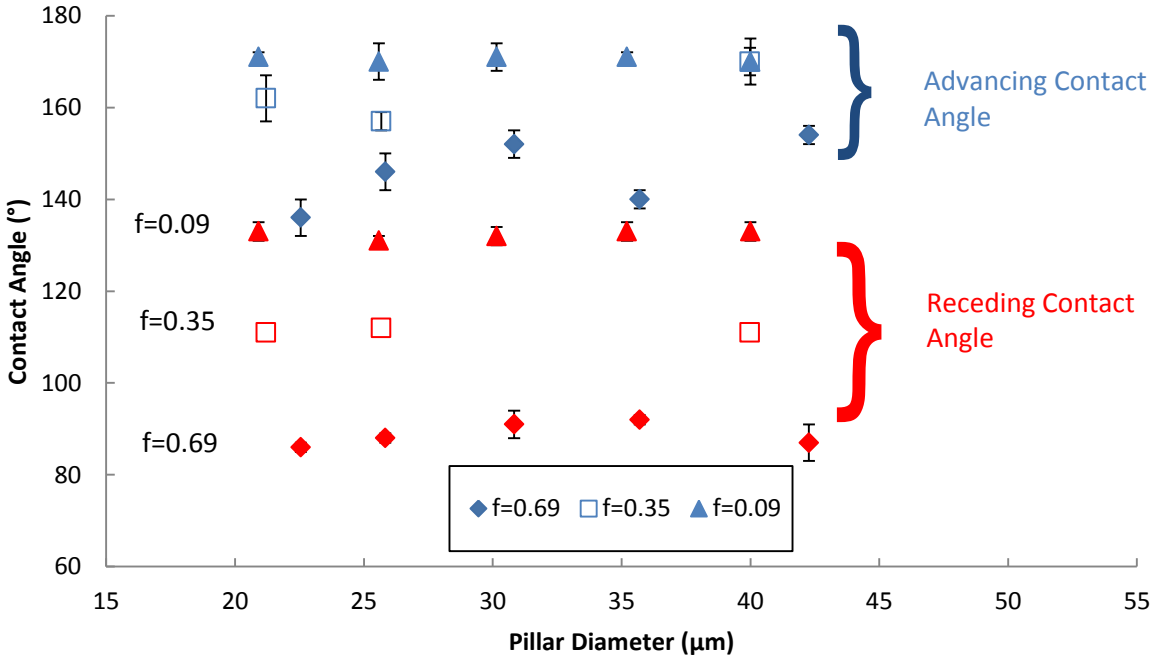

Figure 2-8 – Advancing and receding contact angles for ethylene glycol plotted against pillar diameter, with Cassie fraction kept constant within each set of Cases. Error bars are either within the symbols or are shown

Figure 2-9 shows the raw data for measured advancing and receding contact angles for ethylene glycol plotted against Cassie fraction, with the measurements from the smooth surface reported at $f = 1$ with cross symbols. The solid line represents the predicted Cassie contact angle generated from Equation 2-5.

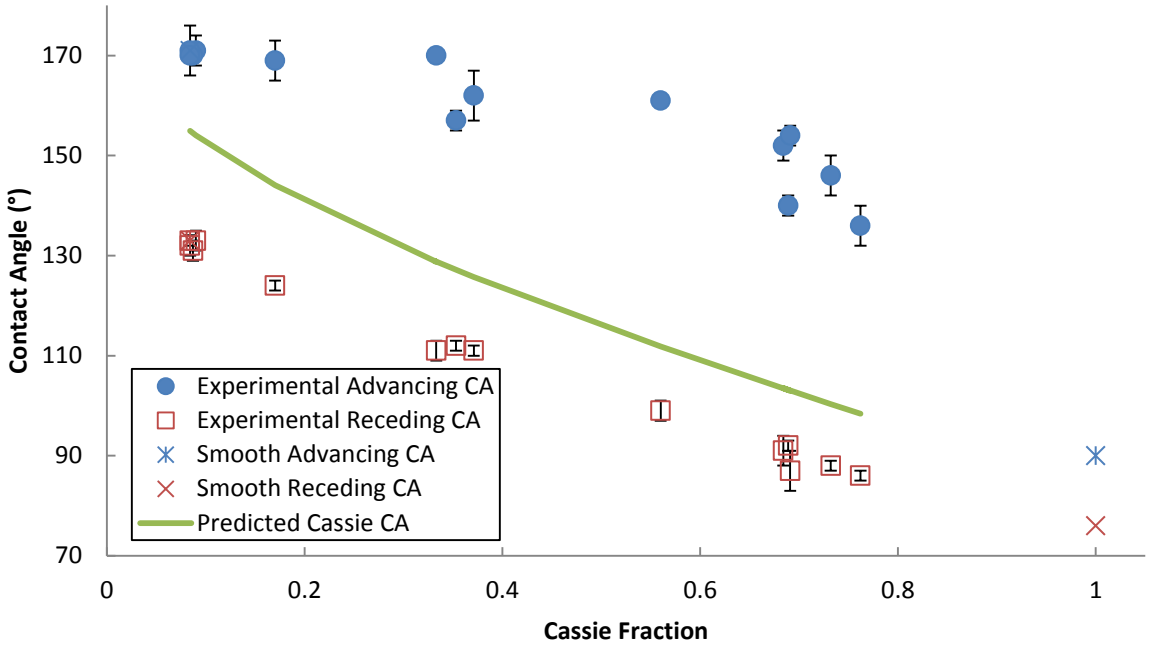

Figure 2-9 – Experimental advancing and receding contact angles for ethylene glycol compared with the equilibrium prediction generated by Equation 5. Error bars are either within their symbols or are shown

The non-dimensional pinning forces for ethylene glycol were determined for the receding contact angles using Equation 2-22 and for the advancing contact angles using Equation 2-23, and the results are plotted versus Cassie fraction in Figure 2-10. As with water, $\frac{F_{P_{Adv,rough}}}{\gamma^{LV}} \neq \frac{F_{P_{Rec,rough}}}{\gamma^{LV}}$. For the Cases where f < 0.33 it is possible the discrepancy can be explained by the system reaching the limiting value of – 1 in Equation 2-20 and being unable to express the full strength of the pinning force. However, for Cases with f > 0.33 the limit in Equation 2-20 cannot explain the discrepancy and the results clearly show the advancing pinning force to be larger than the receding pinning force. As can be seen, the pinning force values for the receding contact angles all fall within the same range, with the average value of $\frac{F_{P_{Rec,rough}}}{\gamma^{LV}}$ being 0.23 ± 0.02, which can be used to create the empirical equation

$$\cos\theta_{C_{Rec,rough,EG}} = (\cos\theta_Y + 1)f - 0.77 \qquad [2\text{-}28]$$

Linear regression of the advancing contact angle pinning forces produces the empirical equation

$$\cos\theta_{Adv,rough,EG} = (\cos\theta_Y + 1)f - (0.8549f + 0.0232) - 1 \qquad [2\text{-}29]$$

The empirical Equations 2-28 and 2-29 are plotted together with the experimental data versus Cassie fraction in Figure 2-11.

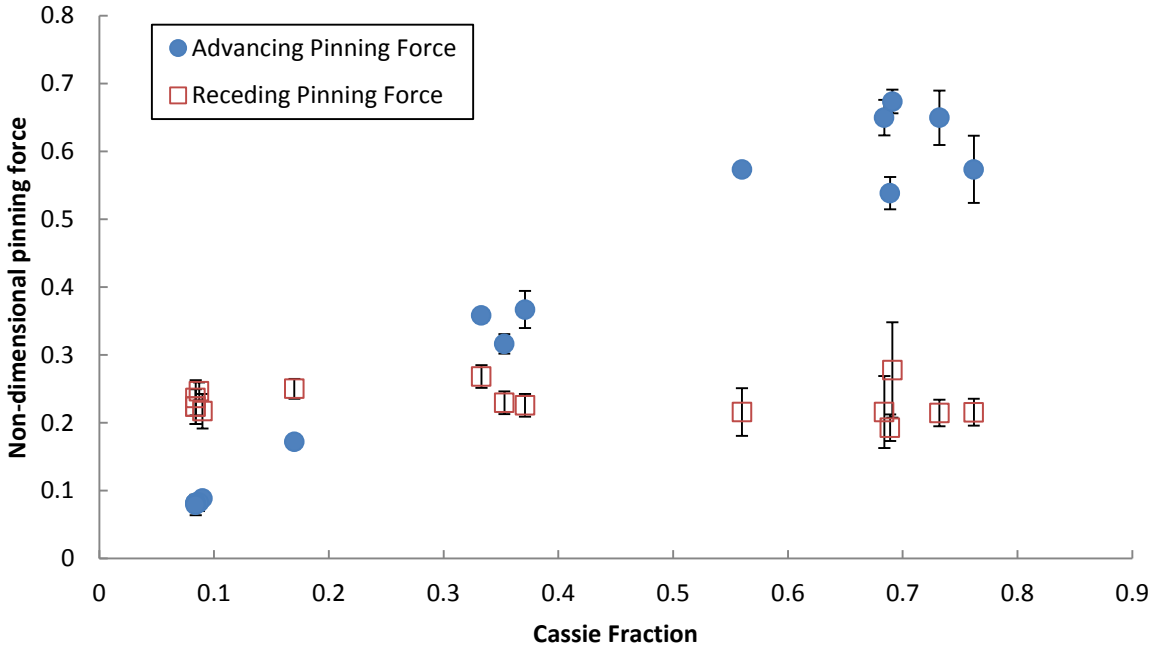

Figure 2-10 – Comparison between the determined advancing non-dimensional pinning forces ($\frac{F_{P_{Adv,rough}}}{\gamma^{LV}}$) and the receding non-dimensional pinning forces ($\frac{F_{P_{Rec,rough}}}{\gamma^{LV}}$) for ethylene glycol plotted versus Cassie fraction

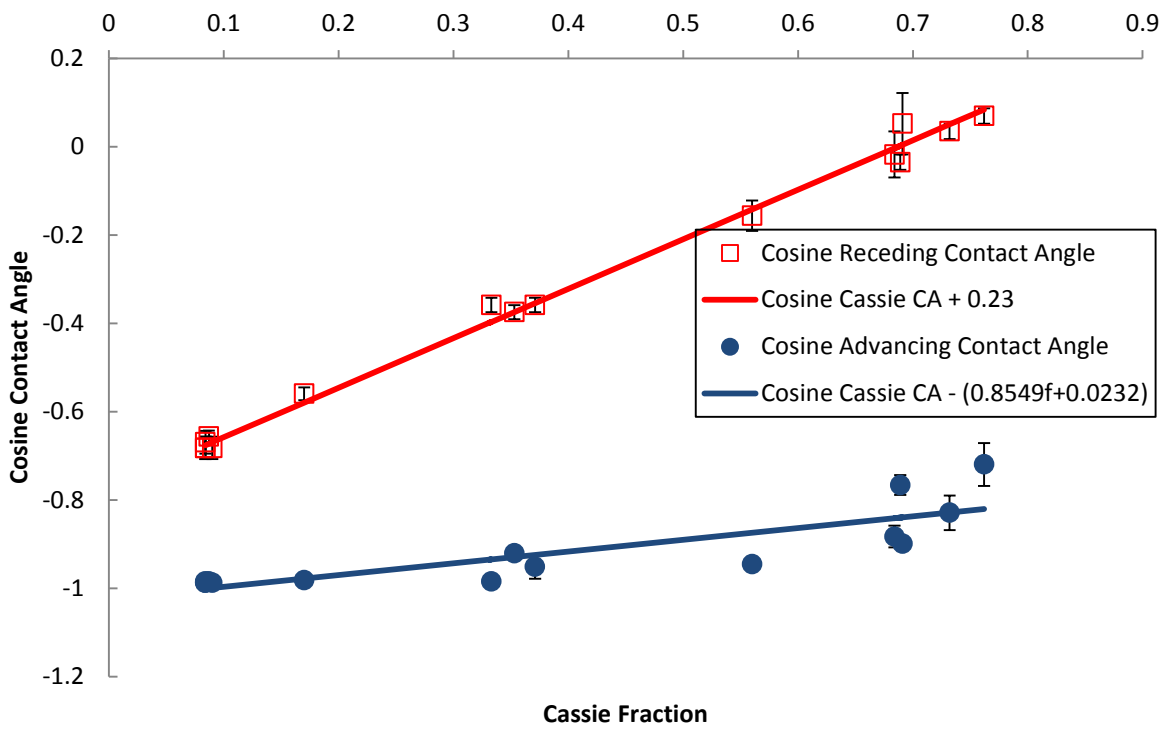

Figure 2-11 – Cosine experimental contact angles compared with empirical predictive equations plotted against Cassie fraction for ethylene glycol

2.4.3 Comparison between systems

When comparing between water and ethylene glycol, for the receding pinning forces we have $\frac{F_{P_{Rec_{Water}}}}{\gamma_{Water}^{LV}} = 0.2$ and $\frac{F_{P_{Rec_{EG}}}}{\gamma_{EG}^{LV}} = 0.23$, which brings up the possibility that the non-dimensional values are in fact statistically the same. Performing a t-test on the different values shows that there is a statistically significant difference ($p < 0.05$) and thus the non-dimensional pinning force values are indeed different for different liquids.

The data of Priest *et al.*[27] for their hydrophobic pillars show general agreement with our experimental results. Our work agrees strongly with their advancing results but only qualitatively with their receding results; although we note that Priest *et al.* were using a significantly different measurement technique that involved sliding their surfaces beneath a pinned drop of constant volume until the leading and

trailing edges assumed constant contact angles. This methodology is more analogous to a tilted plate experiment than to the volume increase and decrease methodology we used, and it has been previously shown that tilted plate and volume change methodologies do not always produce the same results.[56]

In recent papers Butt et al.[19,21] discuss different mechanisms contributing to contact angle and how liquids can pin and impale upon surface roughness from a microscopic perspective. They argued that the apparent advancing and receding pinning forces would be related to contact angle in different ways, as we also found. There the receding contact angle was found to be dependent upon geometric factors (in our nomenclature, a high ratio of x/d is desired rather than a low Cassie fraction) and the intrinsic receding contact angle. However, the calculated advancing contact angle was so high that it could only form an upper bound. This is because it was unlikely this value could ever be reached before outside interference such as thermal or mechanical fluctuation moved the contact line forward and created a lower apparent advancing contact angle. This is similar to our experimental findings, in particular that the advancing contact angle is mostly independent of geometry and is simply very high for these surfaces. The findings of Butt et al. are primarily of a theoretical, microscopic scope in contrast with our primarily experimental, macroscopic scope although their work with confocal microscopy is of interest to advancing how the two modes of thought can be bridged

2.5 – Summary

Photolithographically patterned hydrophobic surfaces were fabricated with various pillar diameters and pillar spacing for three different values of Cassie fraction. Advancing and receding contact angles of both water and ethylene glycol were measured on each of the micro-textured surfaces. For the surface geometry and chemistry chosen, and for both liquids, there was no appreciable difference in contact angle between Cases of similar Cassie fraction but different pillar size and spacing, for both advancing and receding contact angles. A theoretical framework has been developed by which advancing and

receding contact angles are understood as being different from the equilibrium Cassie contact angles due to the presence of additional pinning forces. The framework gives new insight into the behavior of contact angle hysteresis on such textured surfaces. For the surfaces fabricated, it has been shown that the pinning forces for two different liquids (water and ethylene glycol) behave similarly, in that the advancing and receding pinning forces are different functions of Cassie fraction, with receding contact angles having a constant non-dimensional pinning force while the advancing non-dimensional pinning force increases with increasing Cassie fraction. Since we have shown that advancing and receding pinning forces would need to be equal for cosine averaging to be theoretically justified, these results show that cosine averaging cannot be used for any of these systems, not even a cosine averaging scheme incorporating different weights for advancing and receding contact angles, since advancing and receding pinning forces are different functions of the Cassie fraction. While the empirical formulas found in this work are only applicable to systems of our geometry and chemistry and the developed framework can only be applied to systems where the Cassie fraction is already known, further research into other systems, including systems with disordered defects, such as those studied by Butt *et al.*[19] should be motivated by this work.

Chapter 3 : Wetting of Rough Surfaces by a Low Surface Tension Liquid

3.1 – Introduction

In the context of the study of wetting behavior textured surfaces are those surfaces that have three-dimensional features that alter the behavior of liquid contact angle. Ability to define contact angles is important in numerous fields to achieve properties such as self-cleaning and anti-fouling surfaces,[37] where extremely high or extremely low contact angles are frequently desired over intermediate values, or for potential sensor applications where changing concentrations of surfactants can be predicted on defined surfaces.[78]

In Chapter Two we examined with both theory and experiment the applicability of introducing additional non-dimensional pinning forces to equilibrium equations of contact angle for smooth and non-penetrated wetting surfaces, i.e. the Young and the Cassie equations, respectively. This allowed for capture of the behavior of rough, high-contact-angle surfaces with contact angle hysteresis (*i.e.* the difference between the advancing (θ_{Adv}) and receding (θ_{Rec}) contact angles). We began with the Young equation for contact angles on smooth, chemically homogeneous surfaces

$$\gamma^{LV}\cos\theta_Y = \gamma^{SV} - \gamma^{SL} \qquad [3\text{-}1]$$

where γ^{LV}, γ^{SV}, and γ^{SL} are the interfacial tensions of the liquid–vapor, solid–vapor, and solid–liquid interfaces, respectively. These interfacial tensions are in units of force per unit length or energy per unit surface area, the equivalence allowing for useful thermodynamic arguments. The Young contact angle, θ_Y, is the equilibrium contact angle and does not describe either the advancing or receding contact angles. To this force balance we introduced an additional pinning force term to account for opposition of motion of the contact line across a surface, stemming from all possible sources and combination of

sources. The sign of the pinning force term accounts for the direction of motion. For example, for receding contact angles on a smooth surface when pinning force per unit length (F_P) was added, we proposed:

$$\gamma^{LV}\cos\theta_{Rec} = \gamma^{SV} - \gamma^{SL} + F_P \qquad [3\text{-}2]$$

Rearranging and substituting in the definition of $\cos\theta_Y$ from Equation 3-1 yields:

$$\cos\theta_{Rec} = \cos\theta_Y + \frac{F_P}{\gamma^{LV}} \qquad [3\text{-}3]$$

Assuming for smooth surfaces a pinning force for advancing contact angles that is equal in magnitude but opposite to that for receding contact angles gave:

$$\cos\theta_{Adv} = \cos\theta_Y - \frac{F_P}{\gamma^{LV}} \qquad [3\text{-}4]$$

Adding Equations 3-3 and 3-4 results in:

$$\cos\theta_Y = \frac{(\cos\theta_{Adv} + \cos\theta_{Rec})}{2} \qquad [3\text{-}5]$$

Equation 3-5 is the formula for cosine averaging, a method found in literature[58,79] to approximate the equilibrium Young contact angle from advancing and receding contact angles from experiment. Cosine averaging has experimental validation, although sometimes equal weighting cannot be given to advancing and receding states on some surfaces,[58] and some authors prefer to use averages of angles rather than cosines of angles.[80] From our theoretical and experimental work[81] we find preference for Equation 3-5 when dealing with smooth surfaces.

We then expanded the theoretical framework to rough surfaces with non-penetrated wetting states, also known as Cassie wetting. For systems where the liquid does not penetrate into roughness, the apparent, macroscopic contact angles, θ_C, are described by the Cassie equation,[62] expressed here for textured surfaces with planar tops as:[28]

$$\cos\theta_C = (\cos\theta_Y + 1)f - 1 \qquad [3\text{-}6]$$

where f is the Cassie fraction, which for flat topped feature geometry is the area in contact with solid surface divided by the total projected area of the drop in contact with the solid and with air.

We found from the experimental evidence in Chapter Two, that the advancing and receding pinning forces are not equal in magnitude for surfaces with roughness; thus for advancing and receding contact angles in the Cassie state we proposed the following equations:

$$\cos\theta_{Rec,Cassie} = (\cos\theta_Y + 1)f - 1 + \frac{F_{P_{Rec,Cassie}}}{\gamma^{LV}} \qquad [3\text{-}7]$$

$$\cos\theta_{Adv,Cassie} = (\cos\theta_Y + 1)f - 1 - \frac{F_{P_{Adv,Cassie}}}{\gamma^{LV}} \qquad [3\text{-}8]$$

For the surfaces and liquids examined in Chapter Two for receding contact angles we found that the empirically-determined receding pinning force was constant with changing Cassie fraction, while the empirically-determined advancing pinning force increased linearly with increasing Cassie fraction. The net effect of this is that the receding contact angles show a constant shift below their predicted equilibrium Cassie value, while the advancing contact angles remained at large values and did not change with changing Cassie fraction. These behaviors, a constant advancing contact angle and a shifted receding contact angle, have been observed in past literature.[26,29,6,27]

It is to be emphasized that "pinning" is an empirical term that includes all possible microscopic sources of contact angle hysteresis combined into a single macroscopic term. From the energy defects proposed by Joanny and de Genne[7] to local microscopic conformation of contact angle producing a different apparent macroscopic contact angle as detailed by Wolansky and Marmur[18] to edge pinning[44], all possible sources of deviation from expected behavior are simultaneously captured within the term $\frac{F_P}{\gamma^{LV}}$.

As the surface tension of liquids decrease, the Cassie state becomes increasingly unfavourable.[36] An area of research in maintaining the Cassie state for low surface tension alkanes such as hexadecane to

produce superoleophobic surfaces has received considerable attention recently. A significant contribution to this field was done by Tuteja *et al.,*[42,43] who showed that one particular design of surface texture, a cap on top of a pillar of lesser diameter, can allow for liquids such as hexadecane to remain in the Cassie state. This geometry is however not necessary for superoleophobicity, as the main determining factor is the pinning at the edge of the pillars.[44]

While the behavior of liquids on surfaces when they are wetting in the Cassie state is typified by very high contact angles and low contact angle hysteresis, if the liquid penetrates fully into the roughness of the surface then it enters into the Wenzel state, where the liquid is in full contact with the surface and there is no gas underneath the bulk of the drop. When this happens the Wenzel equation[3] is used

$$\cos\theta_W = r\cos\theta_Y \qquad [3\text{-}9]$$

where *r* is the Wenzel roughness factor which is defined as the actual area of solid in contact with the liquid divided by the projected contact area of the drop bounded by the contact line. While the contact angles in the Wenzel state can theoretically range between 0° and 180°, for very high intrinsic contact angles the Cassie state becomes more favorable[36,35] and thus the Wenzel state is most associated with intermediate and low intrinsic contact angles. In particular, for a surface with a smooth contact angle less than 90°, a sufficiently high roughness should produce an apparent contact angle of 0°. However, in experiments with hydrophilic surfaces with texture, Dorrer and Rühe[30] found that for the advancing contact angles they can obtain values exceeding 120° even when the Wenzel equation predicted values much less than that, including values of 0°. However, they also found that the receding contact angles were at 0°. In characterizing perfluorosulphonic acid membranes Zawodzinski *et al.*[31] found that for intermediate water contents the receding contact angles trended to 0° whereas the advancing contact angles remained above 100°. For such behavior, there is little comprehensive discussion in the literature.

There is however an even more extreme version of the above type of behavior, the so called "sticky superhydrophobic" state. Although the nomenclature has been contested,[82,83] the phenomenon has been observed wherein drops with advancing contact angles greater than 150° also display extreme contact angle hysteresis and low mobility, such as in the work by Balu *et al*.[33] At the greatest extent of this phenomenon a drop with a contact angle of 150° can be suspended from an inverted surface, such as in the work of Peng *et al.*[12] Sometimes called the petal effect, it has been theorized by Feng *et al*.[34] that this phenomenon arises from penetration of microscopic features by the liquid, as in the Wenzel state, while nanoscopic features retain a small amount of air trapped within, as with the Cassie state.

While the mechanisms at work for various forms of extreme contact angle hysteresis systems may not be the same, the pinning force framework from our previous study does offer a possible explanation. Since the pinning forces act in opposition to the motion of the contact line, an extremely rough surface with the liquid in full contact would present a highly convoluted path to advance across. This should manifest as an increased advancing pinning force and thus an increased advancing contact angle.

In our prior work, in which we studied contact angles and contact angle hysteresis on textured surfaces we used water and ethylene glycol as our test fluids, with both remaining in the Cassie state. In this chapter we shall examine the behavior of hexadecane on the same textured surfaces. With a lower surface tension and thus a lower intrinsic contact angle, the use of hexadecane allows for wetting behavior in the Wenzel state, enabling us to examine the expanded validity of the previously developed pinning force framework and extending the concept of an empirically determined pinning force to systems in the Wenzel state. Using the newly expanded framework, we will also examine if there is a relationship between high roughness surfaces and extreme contact angle hysteresis behavior.

3.2 - Proposed Pinning Force Framework for Wenzel Wetting

Herein, our framework will be extended from smooth and non-penetrated wetting surfaces to fully wetting surfaces where the equilibrium contact angle behavior is described by the Wenzel equation. Adding the pinning force terms for advancing and receding liquid fronts, we propose the following equations for the observed advancing and receding contact angles:

$$\cos\theta_{Rec,Wenzel} = r\cos\theta_Y + \frac{F_{P_{Rec,Wenzel}}}{\gamma^{LV}} \quad [3\text{-}10]$$

$$\cos\theta_{Adv,Wenzel} = r\cos\theta_Y - \frac{F_{P_{Adv,Wenzel}}}{\gamma^{LV}} \quad [3\text{-}11]$$

One important point that emerges from such pinning force arguments is that since the cosines of contact angles cannot obtain values above 1 or below -1 (contact angles below 0° or above 180°, respectively), the addition of pinning forces can generate unexpected behavior.[81] In particular, for the Wenzel extension proposed here, if $r\cos\theta_Y > 1$, it means that the advancing pinning force can generate contact angles greater than 0° when complete wetting at 0° is expected from the original Wenzel equation. As previously mentioned, this behavior was observed by Dorrer and Rühe[30] on textured surfaces fabricated using photolithography and made hydrophilic via polymer coating.

3.3 - Materials and Methods

The surfaces used in this study were the same ones used for the study involving water and ethylene glycol and a detailed description of the fabrication process can be found in our previous publication.[81] In brief, the surfaces were fabricated in silicon using industry standard photolithography techniques to produce 30 µm tall pillars of circular cross-sectional area. The geometry used consisted of cylindrical pillars of diameter, *d,* and edge-to-edge separation, *s,* arranged in a hexagonal packing arrangement to maximize symmetry and reduce the effects of sharp corners, which results in a Cassie fraction of

$$f = \frac{\pi d^2}{\sqrt{12}(d+s)^2} \quad [3\text{-}12]$$

Seventeen different Cases were fabricated, each with a different combination of pillar diameter and Cassie fraction. While we designed for specific Cassie fractions, another value that is determined from the geometry is the Wenzel roughness, which for surfaces with the above described dimensions, pillar height, *h*, and the assumption of smoothness of all features, is calculated as:

$$r = 1 + \frac{2\pi dh}{\sqrt{3}(d+s)^2} \quad [3\text{-}13]$$

In Equation 3-13, the 1 represents the contribution of the tops of the pillars and the floor of the surface, while the component that is dependent upon the dimensions represents the contribution of the sidewalls of the pillars. However, after inspection with a scanning electron microscope (SEM) of the surfaces, the equation used had to be adjusted, as the as the pillars were etched using the Bosch etch process,[11] which produces scalloped sidewalls. Taking an idealized geometric approach that treats the sidewalls as being a series of stacked, bisected tori gives a scallop-depth-and-number insensitive increase in the roughness of the sidewalls being increased by $\frac{\pi}{2}$, while the roughness contribution from the tops of the pillars and the floor remain constant, modifying Equation 3-13 to instead be:

$$r = 1 + \frac{\pi^2 dh}{\sqrt{3}(d+s)^2} \quad [3\text{-}14]$$

The SEM images of 5 Cases are shown in Figure 3-12, and the dimensions for all Cases, including both the Cassie fraction and Wenzel roughness for each Case calculated from the measured dimensions are given in Table 3-4. Using Equation 3-14 to calculate the Wenzel roughness gives values that should be treated as maximum values, with the true values likely being somewhere between what would be given by Equations 3-13 and 3-14. Figure 3-13 shows a close examination of the scallops on the sidewall and that the true value of the roughness is likely somewhere between the two extremes of smooth sidewalls and the semi-circular troughs of bisect tori. Fortunately, the Cases with the largest possible variance

between the value calculated using Equation 3-13 and the value calculated using Equation 3-14 all fall within regions where the predicted Wenzel contact angle has already reached a minimum value of 0°, as seen in Figure 3-16, and thus the variation has minimal effect on our calculations.

Table 3-4 – Measured final dimensions of the fabricated Cases

Case	Diameter (μm)	Edge-to-edge separation (μm)	Cassie Fraction	Wenzel Roughness
Case 1	22.4±0.3	2.0±0.3	0.762±0.002	7.37
Case 2	25.8±0.7	2.9±0.5	0.732±0.004	6.34
Case 3	30.8±0.2	4.7±0.3	0.684±0.001	5.18
Case 4	35.7±0.7	5.3±0.3	0.689±0.003	4.63
Case 5	42.3±0.3	6.1±0.4	0.692±0.001	4.08
Case 6	26.0±0.6	7.1±0.6	0.560±0.005	5.06
Case 7	21.2±0.3	12.0±0.5	0.371±0.004	4.30
Case 8	25.7±0.3	15.5±0.3	0.353±0.003	3.59
Case 9	30.5±0.4	18.7±0.5	0.349±0.004	3.15
Case 10	34.7±0.8	22.8±0.5	0.331±0.006	2.80
Case 11	40.0±0.3	26.0±0.3	0.333±0.002	2.57
Case 12	25.0±0.2	32.7±0.2	0.170±0.001	2.28
Case 13	20.9±0.4	45.5±0.5	0.090±0.002	1.81
Case 14	25.6±0.2	56.9±0.3	0.087±0.001	1.64
Case 15	30.2±0.2	68.9±0.2	0.084±0.001	1.53
Case 16	35.2±0.2	80.54±0.3	0.084±0.001	1.45
Case 17	40.0±0.4	91.7±0.2	0.084±0.001	1.40

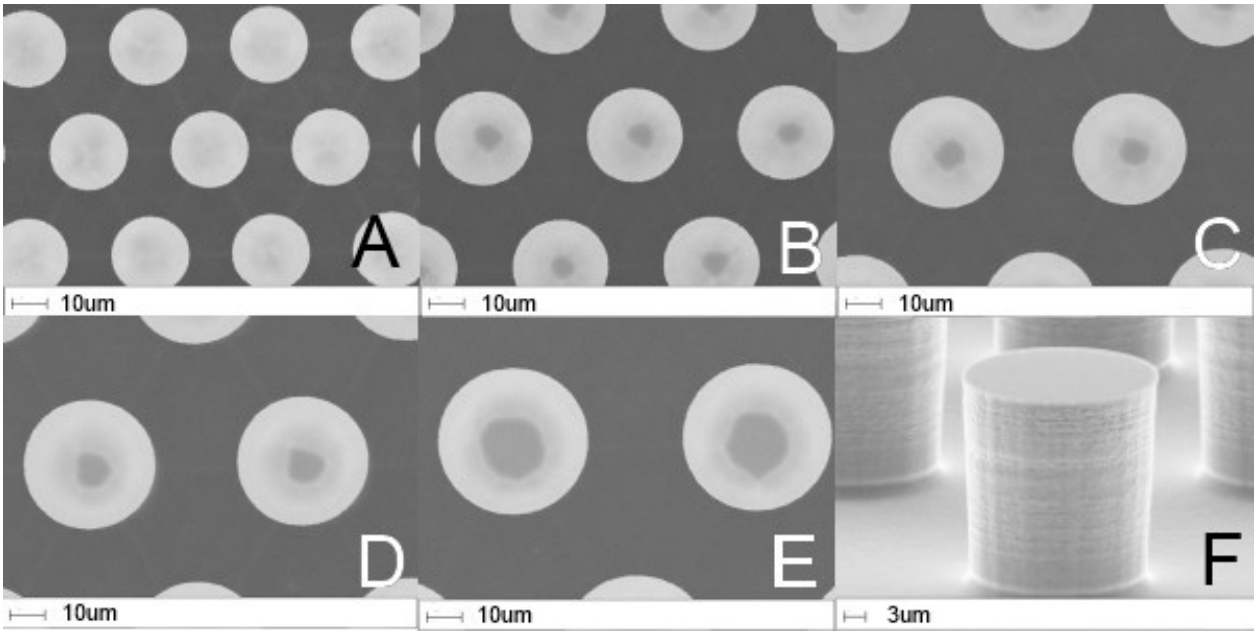

Figure 3-12. Panels A through E show Case 7 through Case 11, respectively, at a 0° top down angle, with pillar diameter increasing from 20 µm to 40 µm while maintaining the same Cassie fraction of approximately 0.35, viewed at a magnification of 3500X. For exact Cassie fraction values see Table 3-4. F shows 25 µm diameter pillars from Case 12, at a 75° angle with a 5000X magnification

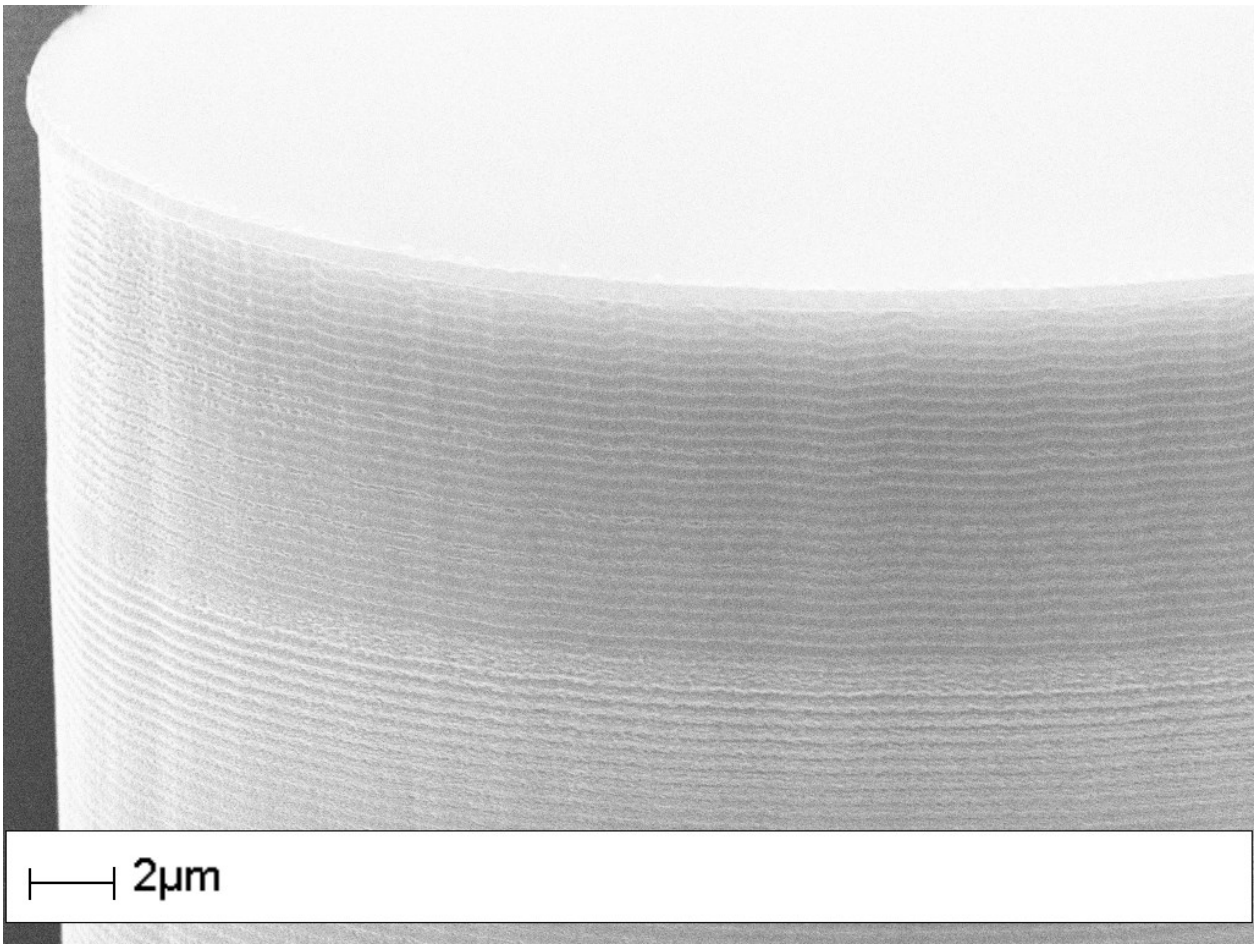

Figure 3-13. SEM image of the sidewall of a single pillar, taken at 10000X magnification and a 75° angle, showing the nanoscale scallops

Contact angles of hexadecane were measured on these surfaces a minimum of three times using a custom optical goniometer that captured images of the drops that were then analyzed using ImageJ[84] and the Drop Snake profile tracing plugin.[85,73] For each measurement set a drop was grown to an initial volume of 25 µL on a surface to confirm that it was situated correctly, and then grown to a final volume of 75 µL at a rate of 0.5 µL/s while taking images. Once at this final volume, the volume was then decreased to 10 µL at the same rate of 0.5 µL/s. Thus we obtained the advancing and receding contact angles, respectively.

3.4 – Results

Of the Cases examined with hexadecane, three were in the Cassie state and the rest were in the Wenzel state. The determination of whether a system was in the Cassie state or the Wenzel state comes primarily from a qualitative examination of drop behavior on the surfaces. For surfaces with Cassie behavior the drops were spheroidal in shape and there was a minimal amount of residue left on the surface after removal. For surfaces with Wenzel behavior the drops spread into the surface texture and conformed to the shape of the unit cell, in this case hexagonal, and required washing to remove not just trace residue but the bulk of the remaining liquid, due likely to the penetration of liquid into the roughness of the textured surfaces. If the drop never had its contact line move while receding then it was considered to have a receding contact angle of 0°.

Because of the differences in behavior we shall separate our discussion of these two states. Which states exhibit Cassie and Wenzel wetting are important as the ones in the Cassie state are all the smallest pillar diameters with Cassie fractions below 0.4.

3.4.1 - Cases in the Cassie State

Figure 3-14 shows the experimental advancing and receding contact angles for the Cases in the Cassie state, along with the contact angles from the smooth surface and the predicted equilibrium Cassie contact angles. The predicted values were generated by estimating the Young contact angle via Equation 3-5 and then using that value in Equation 3-6. As seen in Chapter Two, the Cassie state is characterized by the advancing contact angles being very large, close to the maximum of 180°, and independent of the Cassie fraction while the receding contact angles follow the Cassie equation but with a constant shift from the equilibrium value, indicative of a constant non-dimensional pinning force value.

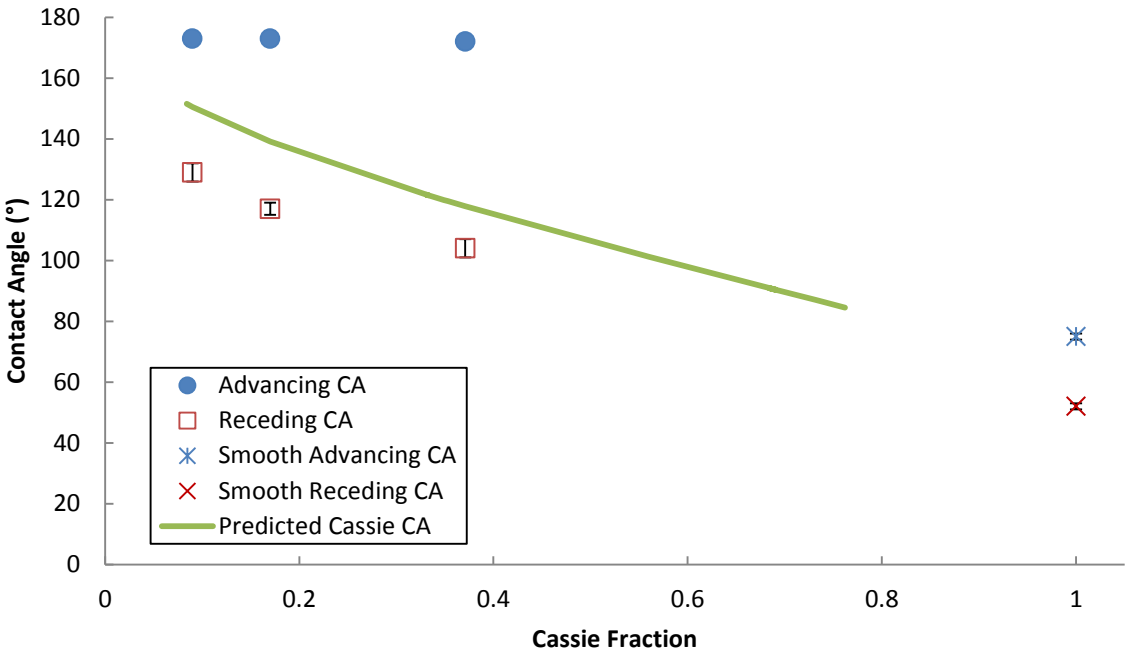

Figure 3-14. Experimental advancing and receding contact angles for hexadecane in the Cassie state, compared to the predicted equilibrium Cassie contact angle that shows the expected behavior for all Cases, if they were in the Cassie state. The advancing and receding contact angles for hexadecane on the smooth surface are shown with cross symbols for comparison. For the advancing contact angles, their error bars are within their symbols.

Following the methodology introduced in Chapter Two, we can compare the data with our proposed framework in Equations 3-8 and 3-9 to determine the pinning forces. Rearranging Equations 3-8 and 3-9 to solve for the non-dimensional pinning forces, yields

$$\frac{F_{P_{Rec,Cassie}}}{\gamma^{LV}} = \cos\theta_{Rec,Cassie} - \left((\cos\theta_Y + 1)f - 1\right) \qquad [3\text{-}15]$$

$$\frac{F_{P_{Adv,Cassie}}}{\gamma^{LV}} = (\cos\theta_Y + 1)f - 1 - \cos\theta_{Adv,Cassie} \qquad [3\text{-}16]$$

The pinning forces determined from the data and Equations 3-15 and 3-16 are shown in Figure 3-15, a near constant receding pinning force and an advancing pinning force that increases with increasing Cassie fraction, confirming for yet another system the utility of the proposed framework from Chapter Two.

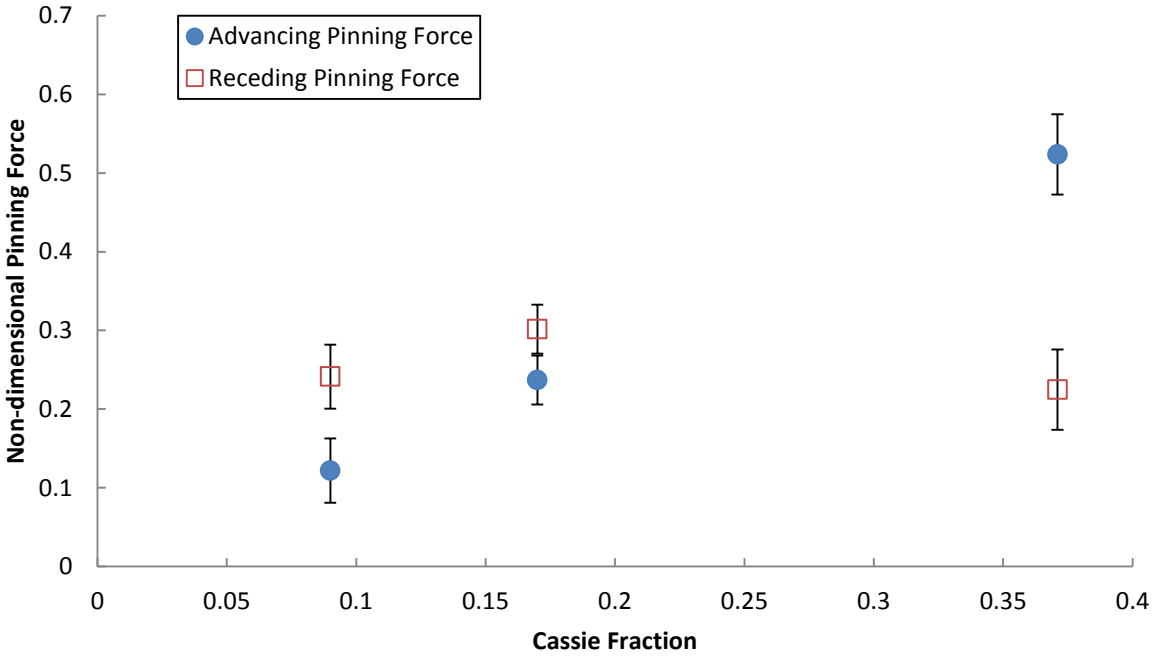

Figure 3-15. Empirically determined advancing and receding non-dimensional pinning forces for the Cases in the Cassie state for hexadecane

3.4.2 - Cases in the Wenzel State

Figure 3-16 shows the experimental advancing and receding contact angles for the Cases in the Wenzel state, along with the predicted Wenzel contact angle calculated by taking the estimated Young contact angle from Equation 3-5 and putting it into Equation 3-10. As seen in the studies mentioned in the introduction, several of these Cases follow non-intuitive behavior where the equilibrium Wenzel contact angle is predicted to be 0° but the measured advancing contact angle is not only above 0° but above 90°. With the advancing contact angle on the smooth surface being below 90° then according to the original Wenzel equation any increase in the Wenzel roughness should serve to decrease the contact angle rather than increase it.

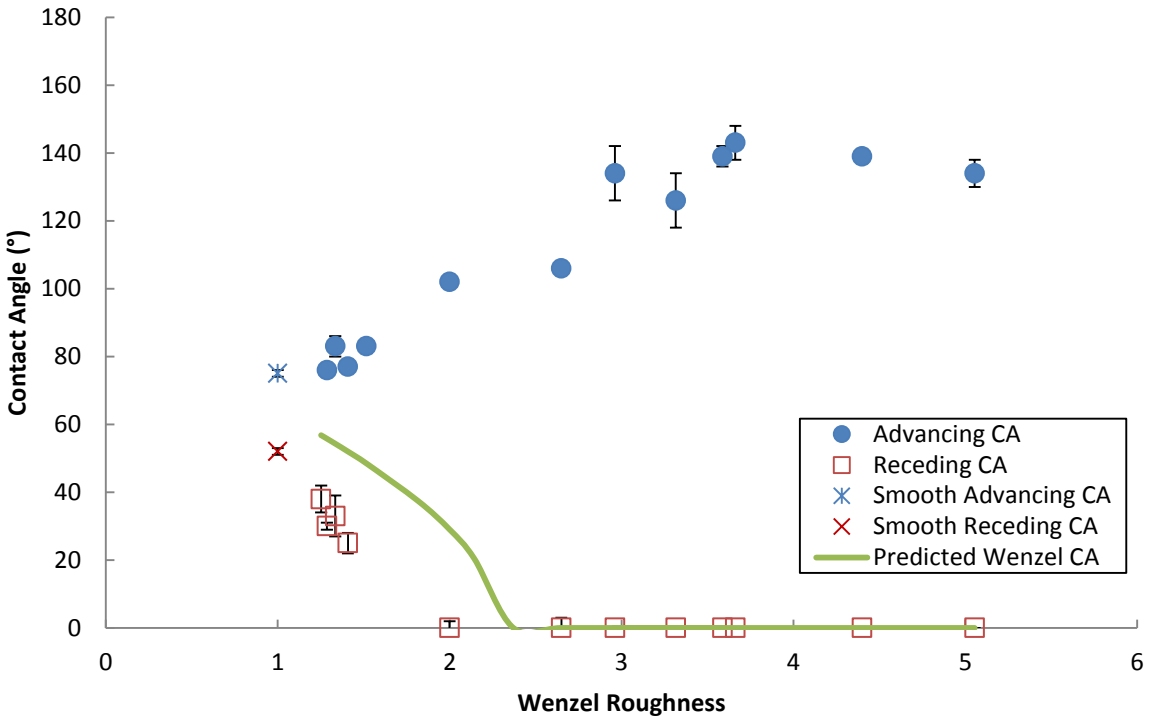

Figure 3-16. Experimental advancing and receding contact angles for hexadecane in the Wenzel state, compared to the predicted equilibrium Wenzel contact angle. The advancing and receding contact angles for hexadecane on the smooth surface are shown with cross symbols for comparison

Equations 3-10 and 3-11 can be rearranged for the non-dimensional pinning forces, yielding

$$\frac{F_{P_{Rec,Wenzel}}}{\gamma^{LV}} = \cos\theta_{Rec,Wenzel} - r\cos\theta_Y \qquad [3\text{-}17]$$

$$\frac{F_{P_{Adv,Wenzel}}}{\gamma^{LV}} = r\cos\theta_Y - \cos\theta_{Adv,Wenzel} \qquad [3\text{-}18]$$

Using experimental values in Equations 3-17 and 3-18 gives the determined advancing and receding pinning forces shown in Figure 3-17. From Figure 3-17 it can be seen that as Wenzel roughness increases the advancing pinning force rapidly grows, up to a plateau value of about 1.8.

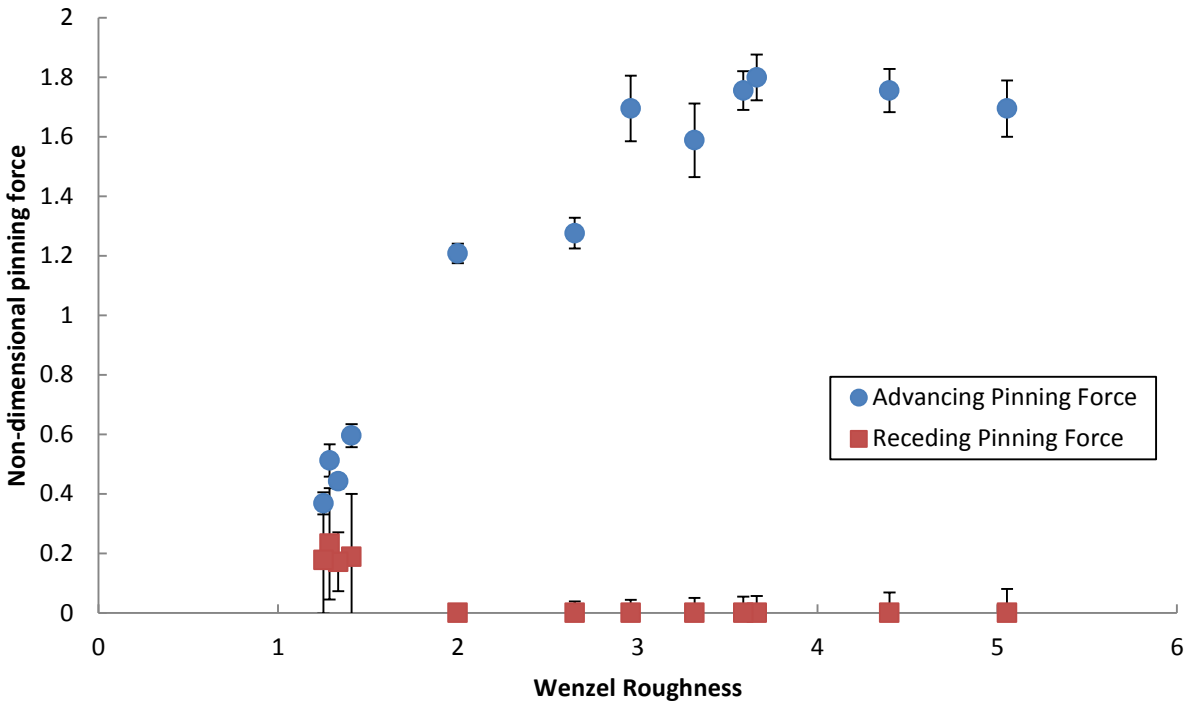

Figure 3-17. Empirically determined advancing and receding non-dimensional pinning forces for the Cases in the Wenzel state for hexadecane

As the non-dimensional pinning forces represent increased difficulty for the motion of the contact line this makes the existence of large advancing contact angles on surfaces with expected Wenzel contact angles of 0° understandable rather than counter-intuitive. This is so as the roughness is providing such a large barrier to the motion of the contact line that it forces the existence of a large advancing contact angle.

While the Cases that demonstrate drops in the Cassie state demonstrate the same behavior as seen by drops of other liquid in the Cassie state, the drops in the Wenzel state demonstrate how extremely strong contact line pinning can generate initially unexpected results.

3.5 – Summary

In this chapter we have examined the wetting behavior of hexadecane upon textured rough surfaces. For cases in which hexadecane remained in the Cassie state, the behavior is similar to that seen on these surfaces with water and ethylene glycol which remained in the Cassie state. However, hexadecane drops also wetted rough surfaces in the Wenzel state (penetrating the roughness). To understand these results we have extended our previous framework of empirically determined non-dimensional pinning forces to the wetting of rough surfaces in the Wenzel state. For the surfaces studied with hexadecane, the existence of non-dimensional pinning forces gives an explanation for the existence of advancing contact angles above 90° on rough surfaces in the Wenzel state when contact angles of 0° are predicted by the ordinary Wenzel equation, in that the contact line pinning is so great it forces the advancing contact angles to assume higher apparent macroscopic values.

Chapter 4 : Study of Model Superoleophobic Surfaces Fabricated with a Modified Bosch Etch Method

4.1 – Introduction

Wettability refers to how a liquid behaves when brought into contact with a surface. Two primary ways of characterizing wettability are repellency and mobility, which are determined by the advancing contact angle and the contact angle hysteresis (the difference between advancing and receding contact angles),[5,86] respectively. Contact angle, θ, is the angle that the liquid-vapour interface makes with the solid surface, measured through the liquid. It arises from free energy minimization[55] or from a force balance of surface tensions at the three-phase contact line, which gives rise to the Young equation

$$\gamma^{LV} \cos\theta_Y = \gamma^{SV} - \gamma^{SL} \qquad [4\text{-}1]$$

where γ^{LV}, γ^{SV}, and γ^{SL} are the interfacial tensions between the liquid, L, vapour, V, and solid, S, and θ_Y is the Young contact angle. The Young equation, Equation 4-1, applies only for ideal smooth surfaces in equilibrium. For non-ideal surfaces, rather than the equilibrium contact angle being seen instead what is observed are advancing and receding contact angles. The advancing contact angle is the contact angle measured when the liquid contact line is moving across a solid surface in unwetted areas, while the receding contact angle is measured when the contact line is moving across a solid surface into areas that have already been wetted. The difference between the advancing and receding contact angle is the contact angle hysteresis

In general, a surface can be characterized as being hydrophobic if it has a water contact angle greater than 90°, and superhydrophobic if it has advancing and receding contact angles greater than 150°. Conversely, a surface with a contact angle of approximately 0°, such as titanium oxide when exposed to light,[87] is said to be superhydrophilic. Usual hydrophilic materials are such materials as silicon dioxide,

with the adherence of water droplets to glass being a common example of hydrophilicity. No known smooth materials can chemically produce water contact angles significantly above 120°, but values approaching 180° are obtainable if a surface has additional roughness. For rough surfaces, there are two models for explaining apparent contact angles, the Wenzel model[3] and the Cassie model.[4] In the Wenzel state the liquid has penetrated into, and is in full contact with, the surface roughness. The roughness, *r*, is the surface area in contact with the liquid divided by the projected area bounded by the circumference of the drop, such that a perfectly smooth surface has a value of *r* = 1, and rough surfaces have r > 1. In the Wenzel state this roughness changes the intrinsic (or Young) contact angle, θ_Y, to the Wenzel contact angle, θ_W, according to

$$\cos\theta_W = r\cos\theta_Y \qquad [4\text{-}2]$$

If on the other hand the liquid is not entirely in contact with the surface (*i.e*. air pockets are trapped in the troughs of a rough surface) then it is in the Cassie state. The area of the drop in contact with the surface divided by the bounded projected area is the liquid–solid interface fraction f_1 and the area not in contact with the surface divided by the bounded projected area is the liquid–vapour interface fraction f_2, giving rise to

$$\cos\theta_C = f_1\cos\theta_Y - f_2 \qquad [4\text{-}3]$$

where the apparent contact angle is the Cassie contact angle, θ_C. In the event of a flat topped surface where $f_1 + f_2 = 1$ the Cassie equation is typically reduced to

$$\cos\theta_C = (\cos\theta_Y + 1)f - 1 \qquad [4\text{-}4]$$

where $f = f_1$, referred to as the Cassie fraction.

Because the Cassie state is a heterogeneous state with gas trapped beneath the drop, it is not necessarily a stable state.[36] The Cassie state can in fact be a metastable state with an energy barrier

existing between it and the Wenzel state, or the transition from the Cassie to the Wenzel state can take sufficiently long that the system appears initially in the Cassie state.

If one can have surfaces that remain in the Cassie state in contact with water as well as oils and other organic liquids of low surface tension, then many applications can be facilated, such as self-cleaning surfaces that are not fouled by oil.[37] Such surfaces are called superoleophobic surfaces, which are surfaces that are highly repellent to oils. Unlike superhydrophobic surfaces, they are not naturally occurring in nature due to the lower surface tensions of oils making them more likely to be in the Wenzel state. Use of microfabrication techniques developed for the semiconductor industry allows for the fabrication of regular arrays of pillar structures that can have unique geometries not seen in nature. One particular design is the so called 'micro-hoodoo' structure pioneered by Tuteja *et al.*[43,42] whereby arrays of micro-pillars fabricated with silicon dioxide caps on top, with greater diameter than the supporting column of silicon underneath, producing overhanging structures. These overhanging structures can increase the stability of the Cassie state as they pin drops at the sharp edge of the cap, requiring additional energy to penetrate into the surface texture, as shown by Fang and Amirfazli.[44]

These micro-hoodoo designs have been further explored by Zhao *et al.*[41] with advancing contact angles of 156° and 158° found for water and hexadecane, respectively. As hexadecane has a much lower surface tension (27.87 mN/m at SATP)[2] in comparison to water (surface tension 71.99 mN/m at SATP),[2] this behaviour of hexadecane having a comparable or even larger contact angle than water is unexpected, but Zhao *et al.* offer no explanation for why the hexadecane should have a contact angle higher than water. However, such structures did demonstrate a large increase in hexadecane contact angle, attributed to the liquid sagging into the void spaces between the pillars decreasing mobility; this was observed by solidifying polyethylene wax on a textured surface and then examining the solid drop under SEM. While Zhao *et al.*[41] only consider the decrease in mobility as arising from this behaviour, from Equation 3, if f_1 remains constant, and f_2 increases, then the apparent contact angle is expected to

increase. Any sagging would involve an increase in the liquid–vapour interfacial area and thus increase the apparent contact angle; however, current evidence shows that sagging behaviour increases drop pinning and thus decreases mobility. This means that even if the intrinsic contact angle decreases there are mechanisms which can allow for increased contact angle.

Any such sagging for a system is however problematic in that if the liquid was to make contact with the floor of a textured surface it would likely cause a transition from the Cassie to the Wenzel state.[88,89,90] To minimize this from occurring, the pillars need to ideally be tall. What precisely is required to be "tall" is related to the geometry of the system in question,[19] but in general the greater the feature-height-to-feature-size ratio, the better. However, for superoleophobic surfaces featuring overhanging cap geometry limits on how tall the pillars can be made are present, as standard fabrication typically involves isotropic etching of silicon underneath a patterned layer of silicon dioxide. The limit of this is the point at which the etch process reaches far enough to cut the cap off in the centre, which for pillars with a circular cross section means that the pillars are limited in height to the radius of the top cap. Since the height has to be greater than the separation between the pillars, this places a lower bound upon the realizable Cassie fraction. As both height and a low Cassie fraction are desired when designing superoleophobic surfaces, a fabrication method that can achieve both is desirable.

One reported alternative to isotropic etching of silicon to form overhang structures is the fabrication of nanonails reported by Ahuja *et al.*[91] These structures involve the Bosch etch process,[92] which involves using alternating applications of fluorine polymer and reactive ion plasma bombardment. The polymer adheres isotropically and prevents etching of the silicon by the reactive ions, but is removed under the directional plasma bombardment, allowing for the reactive ions in the plasma to etch the silicon where the protect polymer has been removed isotropically. This allows for a series of isotropic etches to become an anisotropic etch, allowing for high aspect ratio features to be fabricated. The process creates characteristic scalloped sidewalls as each etch step is an isotropic etch of a few hundred

nanometres at the bottom of the feature. The nanonails take advantage of these scallops by having a silicon cap somewhat larger than twice the scallop depth. This allows for the formation of overhanging caps on pillars with high aspect ratios, but also means that the pillar diameters cannot be designed independently from the process and limits the pillar diameters to a very narrow range.

Our first objective for the work reported in this chapter was to fabricate surfaces with controlled geometry of pillar cross-sectional diameter, pillar separation, and Cassie fraction using a previously unreported modification of the Bosch etching process that will allow for the fabrication of overhanging cap structures. The second objective was to then characterize these surfaces via imaging to confirm that they have the desired features. The third objective was to characterize these surfaces with three different liquids of varying surface tension to determine if these structures show increased contact angles over the smooth surface and a surface with vertical walled pillars with similar Cassie fraction, pillar diameter and surface chemistry. The final objective of this chapter was to examine how the contact angles on these surfaces vary according to the defined geometries and draw conclusions based upon the defined geometries.

4.2 - Materials and Methods

4.2.1 Design

For this study, we wished to perform an examination of the effects of cross-sectional diameter of the pillars, pillar separation, and Cassie fraction on the wetting behaviour of water, oils, and other liquids with varying surface tensions. Since the combination of pillar diameter and spacing determines the Cassie fraction, the three parameters are inter-related. To produce more symmetric drop spreading, a hexagonal pattern with circular pillar cross-sections was used to minimize variation in pillar distance and maximize symmetry, illustrated in Figure 4-1. The two primary design parameters are the pillar cross-

sectional diameter, *d,* and the center-to-center pillar spacing, *x*, which can also be expressed as the sum of the diameter and the edge-to-edge spacing, *s*. Also of importance is the height, *h*, of the pillars.

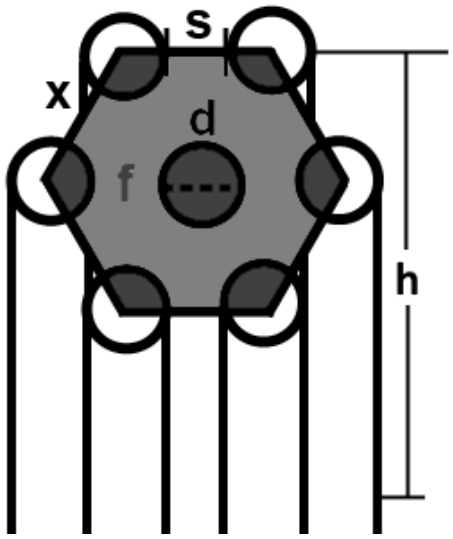

Figure 4-1 – Schematic of a hexagonal unit cell and design parameters

The Cassie fraction on a surface with such geometry is given by

$$f = \frac{\pi d^2}{\sqrt{12}(d+s)^2} \qquad [4\text{-}5]$$

This equation can also be rearranged to solve for a separation that will produce given values of diameter and Cassie fraction. With this design equation, eight different Cases were designed with varying values of *d* and *f.*

Alongside each of the eight textured Cases, a smooth section was included so that intrinsic contact angle could be measured accurately, even if the wafer was later diced and different Cases subjected to different chemical treatments or testing procedures. Because the exterior edges of a silicon wafer are prone to higher rates of damage and greater variation of processing when plasma etched, these smooth surfaces were kept on the exterior of the wafer while the textured portions were clustered toward the

interior and thus the smooth surfaces served a secondary function of protecting the textured surfaces from damage.

4.2.2 Fabrication

The wafer fabrication started with a silicon wafer with a layer of silicon dioxide approximately 500 nm thick, grown by a thermal oxidation process, done at the University of Alberta's NanoFab. This wafer was cleaned of trace organic residue via immersion in a hot piranha bath for 15 minutes. Piranha is a mixture of sulphuric acid at 97% concentration and hydrogen peroxide at 30% concentration mixed at a 3:1 ratio. Once all organic residue was removed the silicon wafer had a layer of hexamethyldisilazane (HDMS) applied to allow better cohesion between the wafer and photoresist. A layer of HPR 504 photoresist (Fujifilm) approximately 1.25 μm thick was applied via spin coating and then soft baked on a hot plate at 115 °C for 90 s before being allowed to sit for 15 minutes to reabsorb moisture from the surrounding air. Once the photoresist stabilized it was patterned with UV light and a mask aligner and the developed photoresist dissolved via 354 developer (Microposit). With the pattern from the mask properly transferred, the exposed silicon dioxide was etched using fluoroform (CHF_3) plasma in a Surface Technology Systems (STS) reactive ion etch machine. The wafer was then transferred to a STS Advance Silicon Etcher High Resonance Magnet (ASE HRM) etcher where it underwent a variation of the Bosch etching recipe.[11] In the standard Bosch etch, sulphur hexafluoride (SF_6) and octafluorocyclobutane (C_4F_8) plasmas alternate, with the SF_6 serving as an isotropic silicon etchant while the C_4F_8 deposits and forms a passivation layer on the sidewalls of the substrate being etched, preventing etching except in the direction of plasma bombardment, creating vertical, scalloped sidewalls. We started with a recipe for a precision Bosch etch, which applies both forms of plasma simultaneously, producing smoother sidewalls at a cost of a slower etch rate and defects forming for etches greater than approximately 10 μm in depth. For this study we developed a custom recipe that started with a precision Bosch etch for 10

minutes, followed by a pure SF_6 plasma for 3 minutes, followed by another 10 minutes of precision Bosch etch. We chose these etch recipe parameters so that we could obtain pillar heights approximately the same as the largest diameter and significantly larger than the smallest diameter, *i.e.*, both large pillar-diameter-to-height ratios and absolute pillar diameters using the same fabrication method for superoleophobic surfaces, something not previously reported. The choice to have the isotropic etch occur midway through the process was so that it could burn off any excess fluoropolymer that had accumulated; thus allowing for a further anisotropic etch. The three minute isotropic etch was to allow for the largest possible undercut without completely etching through the smallest diameter pillars and cutting the caps off.

This process successfully created micropillar arrays of approximately 23 μm in depth with a noticeable undercut geometry, as can be seen in Figure 4-2 and Figure 4-3. Once the etching was completed, the photoresist layer was removed with sequential washes of acetone, isopropyl alcohol, and deionised water, then had a final descum via oxygen plasma in a Branson 3000 barrel etcher for 10 minutes.

After final cleaning the surface was checked with deionized water and found to be completely wetted in the native state. To produce an even, hydrophobic coating, the wafer was exposed to vapour phase trichloro(1H,1H,2H,2H-perfluorooctyl)silane. After silanization the wafer was checked for superhydrophobic behavior using deionised water before and after examination under scanning electron microscope (SEM) and no degradation of chemical passivation was observed due to exposure to the SEM.

4.2.3 Contact Angle Characterization

The coated wafer underwent initial examination for oleophobic behavior by placing drops of hexadecane and visual examination of contact angle. Because of its low surface tension, the behavior of hexadecane would determine if the surfaces fabricated can be considered oleophobic.

With the wafer confirmed to be repellent to hexadecane, its contact angle behaviour was examined using water, ethylene glycol (surface tension 47.99 mN/m at SATP),[2] and hexadecane. The procedure was consistent for all three liquids, with a drop being deposited from a computer-controlled, servo-actuated needle and syringe from a top-down position onto the surfaces in a custom goniometer apparatus. The test drops were initially deposited at a volume of 25 μL before checking that they had formed correctly, with repositioning required at times to ensure that the needle was in the middle of the drop to prevent the drop from sliding off during testing, particularly during receding contact angle measurements. Once the initial volume was established, the drop volume was increased to 75 μL at a rate of 0.5 μL/s while images were taken at a rate of 2 frames per second. Once the maximum volume of 75 μL was attained the process was then reversed, with the volume of the drop decreased to 10 μL at the same rate while taking images at the same rate. To determine whether or not a drop was truly in the advancing or receding states, the contact radius was also measured and only measurements for which the radius was changing were considered valid.

4.3 – Results

4.3.1 Fabrication Results

The wafers were examined from both a top down angle (0°) and an oblique angle (70°) under SEM so that the surface area of the tops of the pillars and the undercut geometries could be examined, respectively. Of the eight patterned Cases on the wafer, six produced usable micro-pillar arrays. One Case showed defects with the tops of pillars occasionally linking together due to being too closely packed, and the contact angle results were such that the surface was deemed non-functional and excluded from consideration. Another Case produced a completely unusable surface that was almost

smooth with sparse holes due to the pattern being too close together on the photomask. A full summary of the dimensions of the six Cases available that were studied is presented in

Table 4-1.

Table 4-1 – Measured dimensions of the tops of the pillars for the oleophobic wafer

	Measured Diameter (μm)	Measured Pillar Edge-to-edge Spacing (μm)	Measured Cassie Fraction
Case 1	20.6	15.4	0.297
Case 2	6.0	3.0	0.403
Case 3	11.1	6.9	0.345
Case 4	15.3	11.7	0.291
Case 5	20.2	5.15	0.571
Case 6	25.6	19.4	0.294

Pillar top diameters greater than 15 μm tend to be within 10% of their desired values, while pillars with diameters of 10 μm and under had significantly greater values than desired. This is primarily attributed to the photomask design, under the assumption that there would be a reduction of diameter between the designed mask and fabricated surfaces. This assumption held true for the pillars greater than 10 μm, but not for those that were smaller, indicating a divide in fabrication regimes unknown from previous projects utilizing these tools. While the loss of two Cases and the unexpected changes in Cassie fraction (due to unexpected pillar diameters) for two others presented difficulties, these results also gave valuable insight into the tools available to use and have already influenced future design decisions[81] to avoid such problems.

Figure 4-2 shows that there are four identifiable modes of etching along the height of the pillar. In section A the silicon is roughly textured and slopes inward, towards the centreline of the pillars. There is then an abrupt pinch forming a 'waist' followed by smooth sidewalls that slope away from the centreline of the pillars in section B. This smooth etching eventually transitions into another rough section of sidewall with vertically orientated jags while still sloping away from the centre, seen in section

C. The final etching mode visible on the pillars in section D is that of smooth, vertical sidewalls aligned with the caps on the pillars. These etching modes are visible for all Cases, as can be seen in Figure 4-3.

The exact causes of each etching regime are currently unknown, but can be speculated upon given their locations. The roughness of section A occurs all within the top half of the pillars, which would be the parts that were etched using standard methods and then exposed to pure SF_6 plasma, so the roughness may have been caused by uneven build-up of fluropolymer along the sidewalls that was then unevenly etched upon exposure to pure plasma. The pinch in section B is likely the greatest extent of fully isotropic etching before anisotropic etching resumed. The jagged features in section C are suspected to be related to silicon grass, nanometre sized defects typically caused by excess buildup of fluorocarbon polymer or from native silicon dioxide.[93] What likely occurred was that the silicon dioxide caps caused a small amount of scattering off their edges, producing an uneven etch, leaving locations for the silicon grass to form. Section D is clearly where normal etching took over once more.

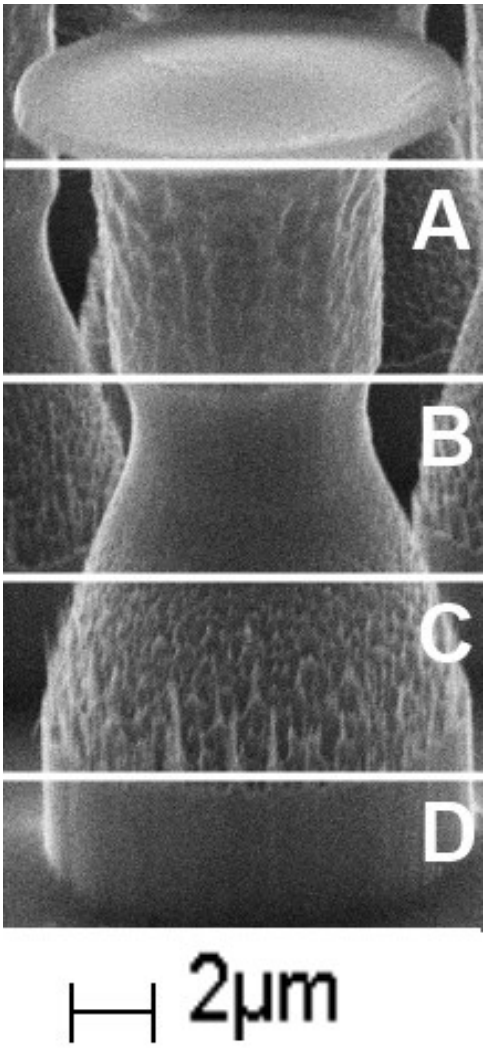

Figure 4-2 – Close up of a pillar from Case 3 at a 70° viewing angle and taken at 5000X magnification, showing the different etching modes present

Figure 4-3 shows SEM images of the undercut geometries of all of the functional Cases, and confirms that silicon grass has formed as instances of the grass structures are visible on the surface floors in the foreground of Cases 1, 4, 5 and 8, seen in Figure 4-3 panels A, D, E, and F, respectively.

All the Cases demonstrate the successful fabrication of overhanging cap structures where the pillar height and diameter are independent, unlike for Tuteja *et al.*'s surfaces[42] or for the nanonails.[91] Of all

the Cases, Case 2, as seen in Figure 4-3 Panel B, shows this by far the most strikingly and prominently with the largest aspect ratio of approximately 4:1 between height and pillar diameter.

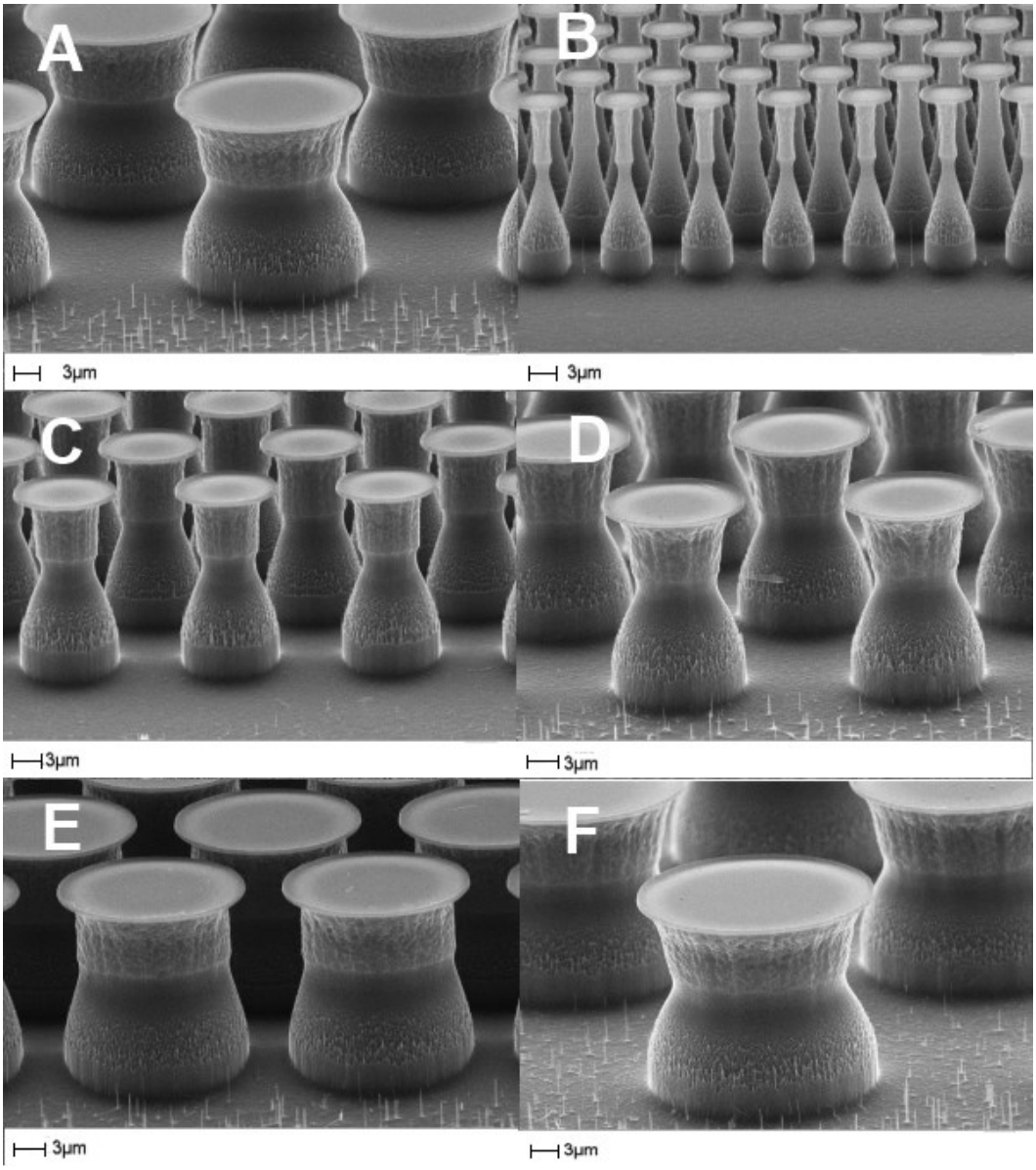

Figure 4-3 - SEM images of the various cases take at a 70° angle, with scale bars shown. Panels are: A, Case 1; B, Case 2; C, Case 3; D, Case 4; E, Case 5; F, Case 6.

4.3.2 Contact Angle Results

Figure 4-4 shows static hexadecane drops on the fabricated surfaces and their elevated contact angles in comparison to the smooth surfaces, demonstrating that the textured surfaces can be considered oleophobic in terms of repellency. Of note is the fact that when rolling off the surface due to tilting from manual manipulation, the hexadecane drops left noticeable wetted trails on the textured portions, thus demonstrating either some degree of collapse into the texture or that the hexadecane remained adhered to the tops of the pillars even after the bulk of the drop had moved on. However, once a hexadecane drop rolled off a textured portion, it remained in the interstitial region between textured surfaces despite the liquid being able to make contact with the bottoms and sides of the pillars. Since contact with the side of the texture should theoretically allow for penetration into the texture more easily than from the top-down direction, we take this as an indication that for these surfaces the oleophobic state was a stable one.

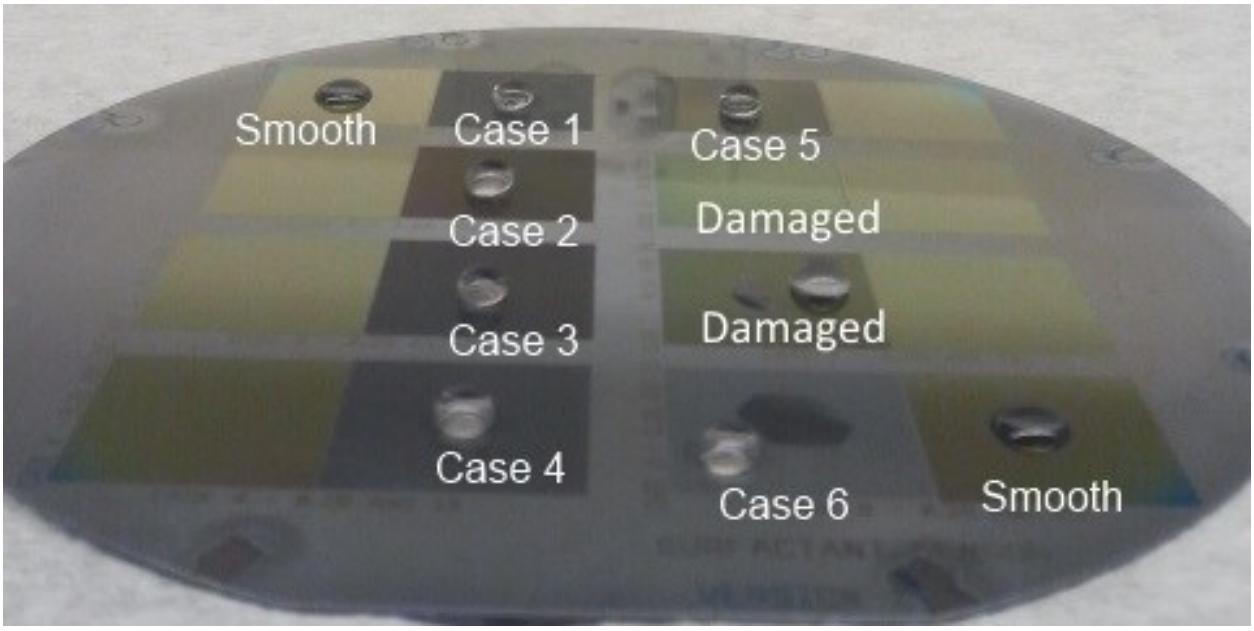

Figure 4-4 – Hexadecane drops on the various textured segements of the wafer, showing their elevated contact angle in comparison to the smooth sections of the surface on the outer portions of the wafer. The interior columns are the textured sections while the exterior columns are the smooth sections.

The results of the contact angle measurements for all three test liquids are summarized in Table 4-2 and show the extreme increases in contact angle the textured surfaces exhibit in comparison to the smooth surface contact angles for both advancing and receding contact angles. However, the increase in contact angles also comes with an increase in contact angle hysteresis. The increase in contact angle hysteresis is greater for lower values of liquid surface tension. This suggests that the increase in repellency is being caused by a decrease in mobility as the contact line pins.

Table 4-2 – Measured advancing and receding contact angles (CA) in degrees for all textured and the smooth surfaces

	Cassie Fraction	Water Advancing CA	Water Receding CA	Ethylene Glycol Advancing CA	Ethylene Glycol Receding CA	Hexadecane Advancing CA	Hexadecane Receding CA
Smooth	1	126.3±0.3	90±1	98±1	61±2	81±2	44±2
Case 1	0.297	170±2	126±1	165±3	106±1	167±3	95±2
Case 2	0.403	167±1	121.7±0.3	153±2	95±1	155±2	89±2
Case 3	0.345	170±2	123±1	161±3	102±1	161±3	96±1
Case 4	0.291	168±2	122±2	165±3	104±1	165±2	98±1
Case 5	0.571	170±1	108±1	153±2	85±1	156±1	74±1
Case 6	0.294	167±2	117±1	166±4	104±1	165±4	97±2

Because the Cassie and Wenzel equations apply to equilibrium states and therefore do not strictly apply to advancing and receding contact angles, the experimental results cannot be used directly in the Cassie or Wenzel equation. In order to make valid predictions and thus comparisons between experiment and theory, a method of determining an equilibrium contact angle value from advancing and receding contact angle is needed. For smooth surfaces, one such method is cosine averaging,[94,79] a method that gives the Young contact angle as

$$\cos\theta_Y = \frac{(\cos\theta_{Adv} + \cos\theta_{Rec})}{2} \qquad [4\text{-}6]$$

While this method gives equal weight to the advancing and receding contact angles, it need not[94] as some surfaces are more accurately modelled by giving unequal weighting to the advancing or receding states, but in general an equal weight model works for most smooth surfaces.

Figure 4-5 shows the advancing and receding contact angles for water on the surfaces plotted against their Cassie fractions, with the solid line showing the behaviour predicted using Equation 4-4, into which an approximate equilibrium Young contact angle generated using Equation 4-6 has been substituted. As can be seen the advancing contact angles remain near constant while the receding contact angles follow the trend predicted by the Cassie equation but with a near constant shift, which is consistent with previous results for simple vertical pillars in the literature[26,29,6] and in our own work as seen in Chapters Two and Three.

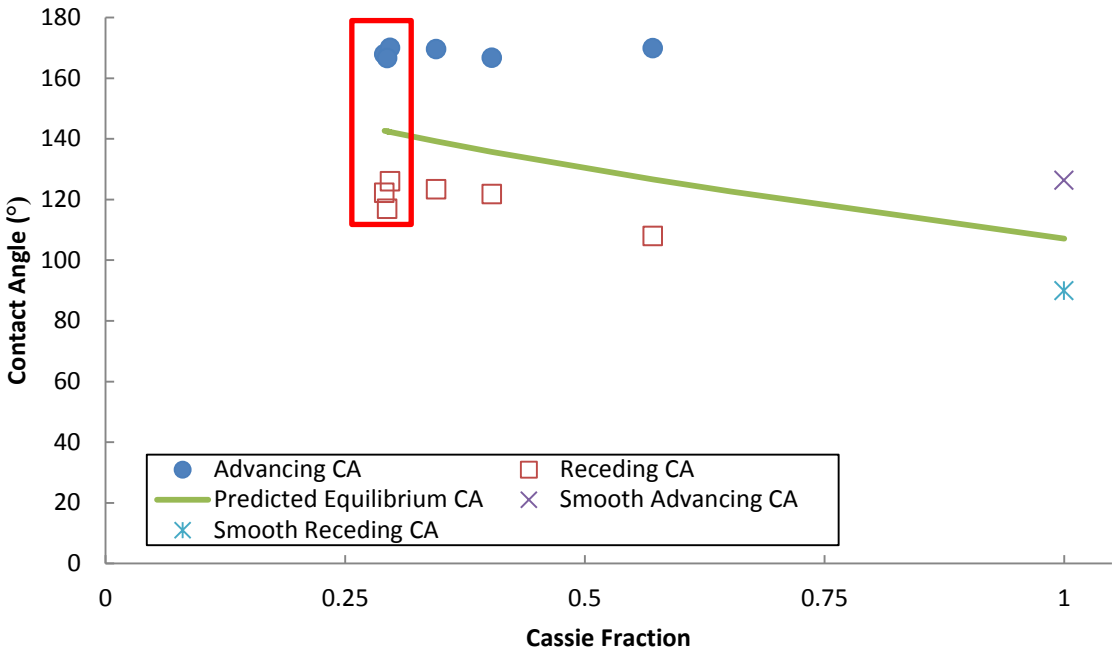

Figure 4-5 – Advancing and receding contact angles for all six Cases versus Cassie fraction for water. Error bars lie within the symbols

Note that there is a trio of Cases with similar Cassie fraction of approximately 0.29, which seem to have different receding contact angles, suggesting an additional factor at play, such as the pillar diameter or spacing. Isolating those three points and plotting against pillar diameter showed no correlation, however.

The results for ethylene glycol produce Figure 4-6, which is similar but unlike with water the advancing contact angles are not constant, having a near constant shift away from the predicted equilibrium line. The exception is for the Case with the highest Cassie fraction, which does not follow that trend and instead remains above 150°, suggesting a minimum advancing contact angle. The receding contact angles however have an even better agreement with being at a constant shift from the equilibrium line.

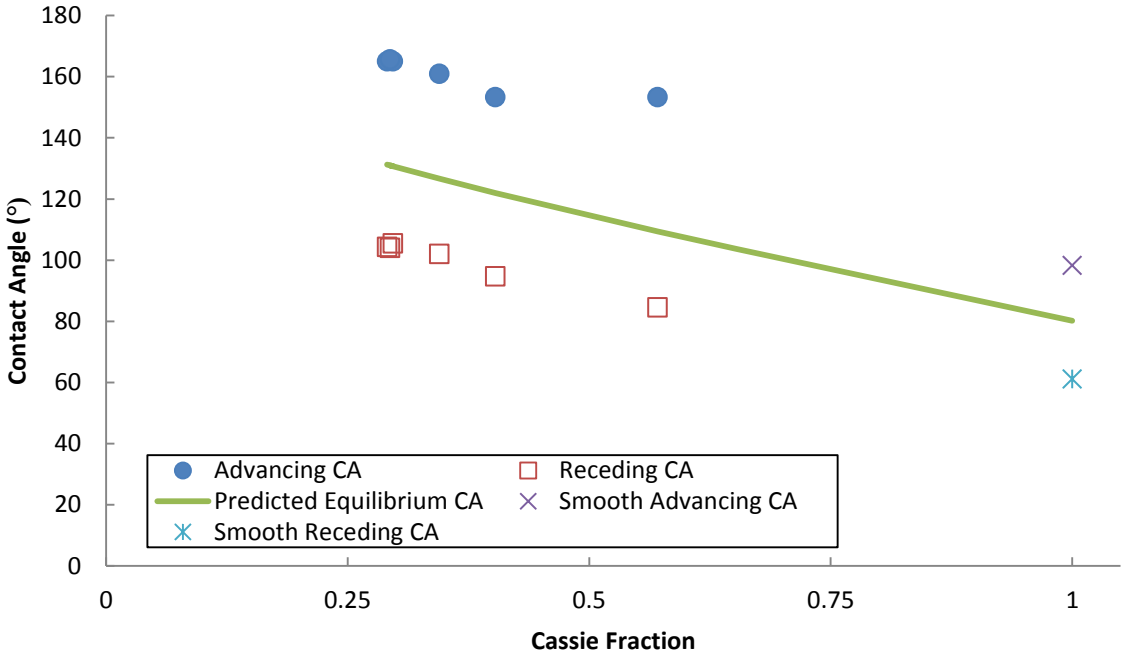

Figure 4-6 – Advancing and receding contact angles for all six Cases versus Cassie fraction for ethylene glycol

Figure 4-7 proceeds from the same methodology as was used for water and ethylene glycol, and while the magnitudes are lower, the behavior shown by hexadecane is similar to that of ethylene glycol, with the advancing contact angles having some sensitivity to the changing Cassie fraction. While the lower magnitudes are expected due to hexadecane's lower surface tension, the advancing contact angles not going beneath 150° is somewhat unexpected. In fact by examining Table 4-2, it can be seen that the advancing contact angles for ethylene glycol and hexadecane are the same.

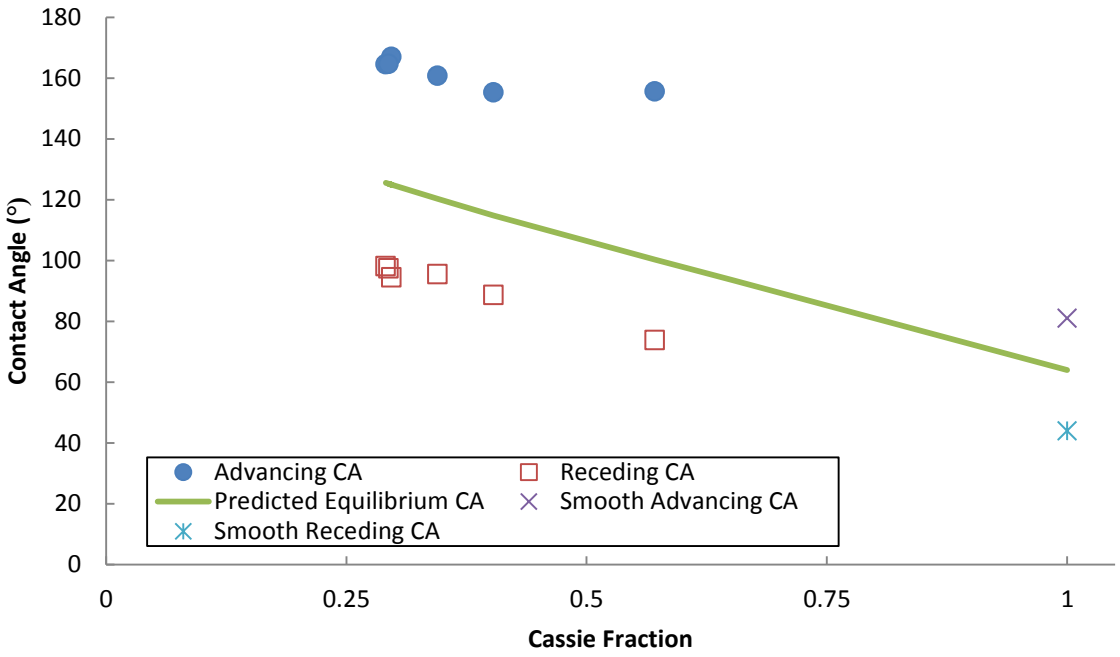

Figure 4-7 – Advancing and receding contact angles for all six Cases versus Cassie fraction for hexadecane

Comparing all of the Cases and liquids used, of particular interest is that the advancing contact angles all remained above 150° even with the use of a dense pillar spacing of f = 0.571. This is particularly important as the advancing contact angle is often the focus for discussion of superoleophobicity. While the advancing contact angles did not respond to changes in surface tension, the receding contact angles did. Examining how the advancing and receding contact angles change with Cassie fraction and surface tension suggests that the surface roughness increases repellency at a cost of decreasing mobility. This can be understood as the Cassie state is maintained by the contact line pinning at the sharp edge of the pillars. However, a limitation of our work is the small spread of Cassie fractions and that there are only three Cases with similar Cassie fraction but varying pillar diameter; this should motivate future work with a more comprehensive spread of parameter values.

In Chapter Two, we developed a pinning force framework[81] to capture empirically the deviation of the experimental advancing and receding contact angles from the Cassie prediction; we can treat the data for superoleophobic surfaces in this work in a similar way. While the full derivation is detailed in Chapter Two, in short we have included pinning forces (with units of force per contact line length) as additional terms that act in opposition to the motion of the contact line. These pinning forces serve to change the advancing and receding contact angles away from the equilibrium value, increasing the advancing contact angles and decreasing the receding contact angles. For drops in the Cassie state and known Cassie fractions the values of the pinning forces can be determined from experimental advancing and receding contact angles as

$$\frac{F_{P_{Rec,rough}}}{\gamma^{LV}} = \cos\theta_{Rec_{Exp}} - \cos\theta_C \qquad [4\text{-}7]$$

$$\frac{F_{P_{Adv,rough}}}{\gamma^{LV}} = \cos\theta_C - \cos\theta_{Adv_{Exp}} \qquad [4\text{-}8]$$

In Chapter Two, we have found that the receding pinning forces remain constant and the advancing pinning forces increase linearly with Cassie fraction. By applying Equations 4-6 and 4-7 to the data in this paper, we find that the same observations hold true for the overhanging cap structures in this work. Table 4-3 summarizes the observed pinning forces for both the vertical sidewall surfaces used previously and the overhanging cap structures used here. We can however only compare Cases in the Cassie state to Cases in the Cassie state, and it must be noted that for the surfaces with vertical sidewalls used for Chapter Two and Three when hexadecane was used only 3 out of 15 of the studied Cases were in the Cassie rather than Wenzel state.

Table 4-3 – Comparison of non-dimensional pinning forces for vertical sidewall textured surfaces and overhanging cap textured surfaces. Note: the vertical sidewall surfaces taken from Chapter Two and Three had only 3 Cases in the Cassie state for hexadecane. Surface tensions are from the CRC Handbook of Chemistry[2] and are all at SATP.

	Vertical Sidewalls	**Overhanging Cap**
Water Advancing (72.99 mN/m)	$0.7933f - 0.0145$	$0.7210f - 0.0265$
Water Receding (72.99 mN/m)	0.20 ± 0.03	0.25 ± 0.06
Ethylene Glycol Advancing (47.99 mN/m)	$0.8549f + 0.0232$	$0.8812f + 0.0447$

Ethylene Glycol Receding (47.99 mN/m)	0.23 ± 0.02	0.41 ± 0.02
Hexadecane Advancing (27.05 mN/m)	$1.4285f - 0.0064$	$1.2157f + 0.0262$
Hexadecane Receding (27.05 mN/m)	0.26 ± 0.04	0.45 ± 0.03

The most immediately telling feature is that the receding pinning forces for ethylene glycol and hexadecane are significantly larger for the surfaces with capped pillars than for the vertical pillars. When comparing the hexadecane results for the vertical sidewalls and overhanging caps between Cases, only one comparable vertical sidewall Case was in the Cassie state while for the overhanging caps all the Cases remained in the Cassie state. Taken together, this indicates that the cap structures increase the stability of the Cassie state, but at the expense of increasing drop pinning.

4.4 – Summary

We have successfully fabricated surfaces with overhanging cap structures using a modification of the Bosch etching technique, including structures where the height of the pillars is significantly greater than the diameter of the caps, allowing for a finer control of geometry in future applications. Advancing and receding contact angles on these surfaces were studied using water, ethylene glycol, and hexadecane, and all liquids demonstrated increased contact angles in comparison to the smooth surface. The overall behaviour of the liquids also conforms to prior experience, with the advancing contact angles tending to remain high and insensitive to changing Cassie fraction while the receding contact angles follow the trends predicted by the Cassie equation much more closely.

Chapter 5 : Conclusions

For Chapter Two, photolithographically patterned hydrophobic surfaces were fabricated with various pillar diameters and pillar spacing for three different values of Cassie fraction. Advancing and receding contact angles of both water and ethylene glycol were measured on each of the micro-textured surfaces. For the surface geometry and chemistry chosen, and for both liquids, there was no appreciable difference in contact angle between Cases of similar Cassie fraction but different pillar size and spacing, for both advancing and receding contact angles. A theoretical framework has been developed by which advancing and receding contact angles are understood as being different from the equilibrium Cassie contact angles due to the presence of additional pinning forces. The framework gives new insight into the behavior of contact angle hysteresis on such textured surfaces. For the surfaces fabricated, it has been shown in Chapters Two and Three that the pinning forces for the three test liquids behave similarly when in the Cassie state. The advancing and receding pinning forces are different functions of Cassie fraction, with receding contact angles having a constant non-dimensional pinning force while the advancing non-dimensional pinning force increases with increasing Cassie fraction. Since we have shown that advancing and receding pinning forces would need to be equal for cosine averaging to be theoretically justified, these results show that cosine averaging cannot be used for any of these systems, not even a cosine averaging scheme incorporating different weights for advancing and receding contact angles, since advancing and receding pinning forces are different functions of the Cassie fraction.

In Chapter Three we have extended the work in Chapter Two to include the behavior of hexadecane drops in the Wenzel state, requiring that we extended the framework of empirically determined non-dimensional pinning forces developed in Chapter Two to the wetting of rough surfaces in the Wenzel state. For the surfaces studied with hexadecane, the existence of non-dimensional pinning forces gives

an explanation for the existence of advancing contact angles above 90° on rough surfaces in the Wenzel state when contact angles of 0° are predicted by the ordinary Wenzel equation, in that the contact line pinning is so great it forces the advancing contact angles to assume higher apparent macroscopic values.

Finally, in Chapter Four we have successfully fabricated surfaces with overhanging cap structures using a modification of the Bosch etching technique, including structures where the height of the pillars is significantly greater than the diameter of the caps, allowing for a finer control of geometry in future applications. Advancing and receding contact angles on these surfaces were studied using water, ethylene glycol, and hexadecane, and all liquids demonstrated increased contact angles in comparison to the smooth surface. The overall behavior of the liquids also conforms to the experiences seen in Chapters Two and Three, with the advancing contact angles tending to remain high and insensitive to changing Cassie fraction while the receding contact angles follow the trends predicted by the Cassie equation much more closely.

We feel that the development of the pinning force framework will greatly improve the understanding of contact angle behavior on rough surfaces demonstrating extreme forms of contact angle behavior and motivate future experiments, discussion, and analysis. In particular surfaces with different pillar cross sectional geometries and packing arrangements and surfaces with different surface chemistries provide a rich ground for exploring how pinning forces are produced. With the addition of the new method developed for producing pillars with undercut geometry, this provides numerous areas to explore experimentally.

Bibliography

(1) Young, T. An Essay on the Cohesion of Fluids. *Philos. Trans. R. Soc. Lond.* **1805**, *95*, 65–87.

(2) Haynes, W. M. *CRC Handbook of Chemistry and Physics*; 94th ed.; CRC Press, 2013.

(3) Wenzel, R. N. Resistance of Solid Surfaces to Wetting by Water. *Ind. Eng. Chem.* **1936**, *28*, 988–994.

(4) Cassie, A. B. D.; Baxter, S. Wettability of Porous Surfaces. *Trans. Faraday Soc.* **1944**, *40*, 546–551.

(5) Pierce, E.; Carmona, F.; Amirfazli, A. Understanding of Sliding and Contact Angle Results in Tilted Plate Experiments. *Colloids Surf. Physicochem. Eng. Asp.* **2008**, *323*, 73–82.

(6) Johnson, R.; Dettre, R. Contact Angle, Wettability, and Adhesion. *Adv. Chem. Ser.* **1964**, *43*, 112–135.

(7) Joanny, J. F.; De Gennes, P. G. A Model for Contact Angle Hysteresis. *J Chem Phys* **1984**, *81*, 552–562.

(8) Pomeau, Y.; Vannimenus, J. Contact Angle on Heterogeneous Surfaces: Weak Heterogeneities. *J. Colloid Interface Sci.* **1985**, *104*, 477–488.

(9) Raphaël, E.; de Gennes, P. G. Dynamics of Wetting with Nonideal Surfaces. The Single Defect Problem. *J. Chem. Phys.* **1989**, *90*, 7577.

(10) Tadmor, R. Line Energy and the Relation between Advancing, Receding, and Young Contact Angles. *Langmuir* **2004**, *20*, 7659–7664.

(11) Guerin, L.; Bossel, M.; Demierre, M.; Calmes, S.; Renaud, P. Simple and Low Cost Fabrication of Embedded Micro-Channels by Using a New Thick-Film Photoplastic. In *International Conference on Solid-State Sensors and Actuators*; 1997; Vol. 2, pp. 1419–1422.

(12) Peng, J.; Yu, P.; Zeng, S.; Liu, X.; Chen, J.; Xu, W. Application of Click Chemistry in the Fabrication of Cactus-Like Hierarchical Particulates for Sticky Superhydrophobic Surfaces. *J. Phys. Chem. C* **2010**, *114*, 5926–5931.

(13) Liu, X.; Wu, W.; Wang, X.; Luo, Z.; Liang, Y.; Zhou, F. A Replication Strategy for Complex Micro/nanostructures with Superhydrophobicity and Superoleophobicity and High Contrast Adhesion. *Soft Matter* **2009**, *5*, 3097.

(14) Artus, G. R. J.; Zimmermann, J.; Reifler, F. A.; Brewer, S. A.; Seeger, S. A Superoleophobic Textile Repellent towards Impacting Drops of Alkanes. *Appl. Surf. Sci.* **2011**, *258*, 3835–3840.

(15) Zheng, L.; Li, Z.; Bourdo, S.; Khedir, K.; Asar, M.; Ryerson, C. C.; Biris, A. S. Exceptional Superhydrophobicity and Low Velocity Impact Icephobicity of Acetone-Functionalized Carbon Nanotube Films. *Langmuir* **2011**, *27*, 9936–9943.

(16) Yang, J.; Zhang, Z.; Xu, X.; Zhu, X.; Men, X.; Zhou, X. Superhydrophilic–superoleophobic Coatings. *J. Mater. Chem.* **2012**, *22*, 2834.

(17) Tsujii, K.; Yamamoto, T.; Onda, T.; Shibuichi, S. Super Oil-Repellent Surfaces. *Angew. Chem. Int. Ed. Engl.* **1997**, *36*, 1011–1012.

(18) Wolansky, G.; Marmur, A. The Actual Contact Angle on a Heterogeneous Rough Surface in Three Dimensions. *Langmuir* **1998**, *14*, 5292–5297.

(19) Butt, H.-J.; Semprebon, C.; Papadopoulos, P.; Vollmer, D.; Brinkmann, M.; Ciccotti, M. Design Principles for Superamphiphobic Surfaces. *Soft Matter* **2013**, *9*, 418–428.

(20) Papadopoulos, P.; Deng, X.; Mammen, L.; Drotlef, D.-M.; Battagliarin, G.; Li, C.; Müllen, K.; Landfester, K.; del Campo, A.; Butt, H.-J.; et al. Wetting on the Microscale: Shape of a Liquid Drop on a Microstructured Surface at Different Length Scales. *Langmuir* **2012**, *28*, 8392–8398.

(21) Butt, H.-J.; Roisman, I. V.; Brinkmann, M.; Papadopoulos, P.; Vollmer, D.; Semprebon, C. Characterization of Super Liquid-Repellent Surfaces. *Curr. Opin. Colloid Interface Sci.* **2014**.

(22) Butt, H.-J.; Vollmer, D.; Papadopoulos, P. Super Liquid-Repellent Layers: The Smaller the Better. *Adv. Colloid Interface Sci.* **2014**.

(23) Öner, D.; McCarthy, T. J. Ultrahydrophobic Surfaces. Effects of Topography Length Scales on Wettability. *Langmuir* **2000**, *16*, 7777–7782.
(24) Reyssat, M.; Quéré, D. Contact Angle Hysteresis Generated by Strong Dilute Defects †. *J. Phys. Chem. B* **2009**, *113*, 3906–3909.
(25) Cansoy, C. E.; Erbil, H. Y.; Akar, O.; Akin, T. Effect of Pattern Size and Geometry on the Use of Cassie-Baxter Equation for Superhydrophobic Surfaces. *Colloids Surf. Physicochem. Eng. Asp.* **2011**, *386*, 116–124.
(26) Dorrer, C.; Rühe, J. Advancing and Receding Motion of Droplets on Ultrahydrophobic Post Surfaces. *Langmuir* **2006**, *22*, 7652–7657.
(27) Priest, C.; Albrecht, T. W. J.; Sedev, R.; Ralston, J. Asymmetric Wetting Hysteresis on Hydrophobic Microstructured Surfaces. *Langmuir* **2009**, *25*, 5655–5660.
(28) Milne, A.; Amirfazli, A. The Cassie Equation: How It Is Meant to Be Used. *Adv. Colloid Interface Sci.* **2012**, *170*, 48–55.
(29) Morra, M.; Occhiello, E.; Garbassi, F. Contact Angle Hysteresis in Oxygen Plasma Treated Poly (tetrafluoroethylene). *Langmuir* **1989**, *5*, 872–876.
(30) Dorrer, C.; Rühe, J. Drops on Microstructured Surfaces Coated with Hydrophilic Polymers: Wenzel's Model and Beyond. *Langmuir* **2008**, *24*, 1959–1964.
(31) Zawodzinski, T. A.; Gottesfeld, S.; Shoichet, S.; McCarthy, T. J. The Contact Angle between Water and the Surface of Perfluorosulphonic Acid Membranes. *J. Appl. Electrochem.* **1993**, *23*, 86–88.
(32) Forsberg, P. S. H.; Priest, C.; Brinkmann, M.; Sedev, R.; Ralston, J. Contact Line Pinning on Microstructured Surfaces for Liquids in the Wenzel State. *Langmuir* **2010**, *26*, 860–865.
(33) Balu, B.; Breedveld, V.; Hess, D. W. Fabrication of "Roll-Off" and "Sticky" Superhydrophobic Cellulose Surfaces via Plasma Processing. *Langmuir* **2008**, *24*, 4785–4790.
(34) Feng, L.; Zhang, Y.; Xi, J.; Zhu, Y.; Wang, N.; Xia, F.; Jiang, L. Petal Effect: A Superhydrophobic State with High Adhesive Force. *Langmuir* **2008**, *24*, 4114–4119.
(35) Marmur, A. Wetting on Hydrophobic Rough Surfaces: To Be Heterogeneous or Not To Be? *Langmuir* **2003**, *19*, 8343–8348.
(36) Li, W.; Amirfazli, A. Microtextured Superhydrophobic Surfaces: A Thermodynamic Analysis. *Adv. Colloid Interface Sci.* **2007**, *132*, 51–68.
(37) Nishimoto, S.; Bhushan, B. Bioinspired Self-Cleaning Surfaces with Superhydrophobicity, Superoleophobicity, and Superhydrophilicity. *RSC Adv.* **2013**, *3*, 671–690.
(38) Bhushan, B.; Jung, Y. C.; Koch, K. Micro-, Nano- and Hierarchical Structures for Superhydrophobicity, Self-Cleaning and Low Adhesion. *Philos. Trans. R. Soc. Math. Phys. Eng. Sci.* **2009**, *367*, 1631–1672.
(39) Kulinich, S.; Farhadi, S.; Nose, K.; Du, X. Superhydrophobic Surfaces: Are They Really Ice-Repellent? *Langmuir* **2011**.
(40) Yin, L.; Xia, Q.; Xue, J.; Yang, S.; Wang, Q.; Chen, Q. In Situ Investigation of Ice Formation on Surfaces with Representative Wettability. *Appl. Surf. Sci.* **2010**, *256*, 6764–6769.
(41) Zhao, H.; Law, K. Y.; Sambhy, V. Fabrication, Surface Properties, and Origin of Superoleophobicity for a Model Textured Surface. *Langmuir* **2011**, *27*, 5927–5935.
(42) Tuteja, A.; Choi, W.; Ma, M.; Mabry, J. M.; Mazzella, S. A.; Rutledge, G. C.; McKinley, G. H.; Cohen, R. E. Designing Superoleophobic Surfaces. *Science* **2007**, *318*, 1618–1622.
(43) Tuteja, A.; Choi, W.; McKinley, G. H.; Cohen, R. E.; Rubner, M. F. Design Parameters for Superhydrophobicity and Superoleophobicity. *MRS Bull.* **2008**, *33*, 752–758.
(44) Fang, G.; Amirfazli, A. Understanding the Edge Effect in Wetting: A Thermodynamic Approach. *Langmuir* **2012**, *28*, 9421–9430.
(45) Barthlott, W.; Neinhuis, C. Purity of the Sacred Lotus, or Escape from Contamination in Biological Surfaces. *Planta* **1997**, *202*, 1–8.

(46) Zheng, L.; Li, Z.; Bourdo, S.; Khedir, K.; Asar, M.; Ryerson, C. C.; Biris, A. S. Exceptional Superhydrophobicity and Low Velocity Impact Icephobicity of Acetone-Functionalized Carbon Nanotube Films. *Langmuir* **2011**.
(47) Antonini, C.; Innocenti, M.; Horn, T.; Marengo, M.; Amirfazli, A. Understanding the Effect of Superhydrophobic Coatings on Energy Reduction in Anti-Icing Systems. *Cold Reg. Sci. Technol.* **2011**, *67*, 58–67.
(48) Barona, D.; Amirfazli, A. A ROBUST SUPERHYDROPHOBIC SURFACE FOR DIGITAL MICROFLUIDICS. In *Proceedings of the ASME 2011 9th International Conference on Nanochannels, Microchannels, and Minichannels*; ASME, 2011.
(49) Bayer, I. S.; Fragouli, D.; Martorana, P. J.; Martiradonna, L.; Cingolani, R.; Athanassiou, A. Solvent Resistant Superhydrophobic Films from Self-Emulsifying Carnauba Wax–alcohol Emulsions. *Soft Matter* **2011**, *7*, 7939.
(50) Lee, S. M.; Kwon, T. H. Effects of Intrinsic Hydrophobicity on Wettability of Polymer Replicas of a Superhydrophobic Lotus Leaf. *J. Micromechanics Microengineering* **2007**, *17*, 687.
(51) Tsujii, K.; Yamamoto, T.; Onda, T.; Shibuichi, S. Super Oil-Repellent Surfaces. *Angew. Chem. Int. Ed. Engl.* **1997**, *36*, 1011–1012.
(52) Artus, G. R. J.; Zimmermann, J.; Reifler, F. A.; Brewer, S. A.; Seeger, S. A Superoleophobic Textile Repellent towards Impacting Drops of Alkanes. *Appl. Surf. Sci.* **2011**.
(53) Morra, M.; Occhiello, E.; Garbassi, F. Contact Angle Hysteresis in Oxygen Plasma Treated Poly (tetrafluoroethylene). *Langmuir* **1989**, *5*, 872–876.
(54) Zhao, H.; Law, K. Y.; Sambhy, V. Fabrication, Surface Properties, and Origin of Superoleophobicity for a Model Textured Surface. *Langmuir* **2011**.
(55) Eslami, F.; Elliott, J. A. W. Thermodynamic Investigation of the Barrier for Heterogeneous Nucleation on a Fluid Surface in Comparison with a Rigid Surface. *J. Phys. Chem. B* **2011**, *115*, 10646–10653.
(56) Pierce, E.; Carmona, F.; Amirfazli, A. Understanding of Sliding and Contact Angle Results in Tilted Plate Experiments. *Colloids Surf. Physicochem. Eng. Asp.* **2008**, *323*, 73–82.
(57) Della Volpe, C.; Siboni, S.; Morra, M. Comments on Some Recent Papers on Interfacial Tension and Contact Angles. *Langmuir* **2002**, *18*, 1441–1444.
(58) Della Volpe, C.; Maniglio, D.; Siboni, S.; Morra, M. An Experimental Procedure to Obtain the Equilibrium Contact Angle from the Wilhelmy Method. *Oil Gas Sci. Technol.* **2001**, *56*, 9–22.
(59) Montes Ruiz-Cabello, F. J.; Rodríguez-Valverde, M. A.; Cabrerizo-Vílchez, M. A. Comparison of the Relaxation of Sessile Drops Driven by Harmonic and Stochastic Mechanical Excitations. *Langmuir* **2011**.
(60) Marmur, A. Soft Contact: Measurement and Interpretation of Contact Angles. *Soft Matter* **2006**, *2*, 12.
(61) Wenzel, R. N. Resistance of Solid Surfaces to Wetting by Water. *Ind. Eng. Chem.* **1936**, *28*, 988–994.
(62) Cassie, A. B. D.; Baxter, S. Wettability of Porous Surfaces. *Trans. Faraday Soc.* **1944**, *40*, 546.
(63) Milne, A.; Amirfazli, A. The Cassie Equation: How It Is Meant to Be Used. *Adv. Colloid Interface Sci.* **2012**, *170*, 48–55.
(64) Johnson, R.; Dettre, R. Contact Angle, Wettability, and Adhesion. *J. Am. Chem. Soc.* **1964**, *43*.
(65) Öner, D.; McCarthy, T. J. Ultrahydrophobic Surfaces. Effects of Topography Length Scales on Wettability. *Langmuir* **2000**, *16*, 7777–7782.
(66) Cansoy, C. E.; Erbil, H. Y.; Akar, O.; Akin, T. Effect of Pattern Size and Geometry on the Use of Cassie-Baxter Equation for Superhydrophobic Surfaces. *Colloids Surf. Physicochem. Eng. Asp.* **2011**.

(67) Dorrer, C.; Rühe, J. Advancing and Receding Motion of Droplets on Ultrahydrophobic Post Surfaces. *Langmuir* **2006**, *22*, 7652–7657.
(68) Dorrer, C.; Rühe, J. Drops on Microstructured Surfaces Coated with Hydrophilic Polymers: Wenzel's Model and Beyond. *Langmuir* **2008**, *24*, 1959–1964.
(69) Joanny, J. F.; De Gennes, P. G. A Model for Contact Angle Hysteresis. *J Chem Phys* **1984**, *81*, 552–562.
(70) Laermer, F.; Schilp, A. Method of Anisotropically Etching Silicon. 5501893, March 26, 1996.
(71) ImageJ http://rsb.info.nih.gov/ij/ (accessed Jun 11, 2013).
(72) BIG>Drop Analysis http://bigwww.epfl.ch/demo/dropanalysis/ (accessed Jun 11, 2013).
(73) Stalder, A. F.; Kulik, G.; Sage, D.; Barbieri, L.; Hoffmann, P. A Snake-Based Approach to Accurate Determination of Both Contact Points and Contact Angles. *Colloids Surf. Physicochem. Eng. Asp.* **2006**, *286*, 92–103.
(74) Mack, G. L. The Determination of Contact Angles from Measurements of the Dimensions of Small Bubbles and Drops. I. The Spheroidal Segment Method for Acute Angles. *J. Phys. Chem.* **1936**, *40*, 159–167.
(75) Extrand, C. W.; Moon, S. I. Contact Angles of Liquid Drops on Super Hydrophobic Surfaces: Understanding the Role of Flattening of Drops by Gravity. *Langmuir* **2010**, *26*, 17090–17099.
(76) Gao, L.; McCarthy, T. J. How Wenzel and Cassie Were Wrong. *Langmuir* **2007**, *23*, 3762–3765.
(77) Extrand, C. W. Model for Contact Angles and Hysteresis on Rough and Ultraphobic Surfaces. *Langmuir* **2002**, *18*, 7991–7999.
(78) Milne, A. J. B.; Elliott, J. A. W.; Zabeti, P.; Zhou, J.; Amirfazli, A. Model and Experimental Studies for Contact Angles of Surfactant Solutions on Rough and Smooth Hydrophobic Surfaces. *Phys. Chem. Chem. Phys.* **2011**, *13*, 16208–16219.
(79) Della Volpe, C.; Siboni, S.; Morra, M. Comments on Some Recent Papers on Interfacial Tension and Contact Angles. *Langmuir* **2002**, *18*, 1441–1444.
(80) Montes Ruiz-Cabello, F. J.; Rodríguez-Valverde, M. A.; Cabrerizo-Vílchez, M. A. Comparison of the Relaxation of Sessile Drops Driven by Harmonic and Stochastic Mechanical Excitations. *Langmuir* **2011**, *27*, 8748–8752.
(81) Koch, B. M. L.; Amirfazli, A.; Elliott, J. A. W. Modeling and Measurement of Contact Angle Hysteresis on Textured High-Contact-Angle Surfaces. *J. Phys. Chem. C* **2014**, *118*, 18554–18563.
(82) Gao, L.; McCarthy, T. J. Teflon Is Hydrophilic. Comments on Definitions of Hydrophobic, Shear versus Tensile Hydrophobicity, and Wettability Characterization. *Langmuir* **2008**, *24*, 9183–9188.
(83) Li, W.; Amirfazli, A. Superhydrophobic Surfaces: Adhesive Strongly to Water? *Adv. Mater.* **2007**, *19*, 3421–3422.
(84) ImageJ http://rsb.info.nih.gov/ij/ (accessed Jun 11, 2013).
(85) BIG>Drop Analysis http://bigwww.epfl.ch/demo/dropanalysis/ (accessed Jun 11, 2013).
(86) Furmidge, C. Studies at Phase Interfaces. I. The Sliding of Liquid Drops on Solid Surfaces and a Theory for Spray Retention. *J. Colloid Sci.* **1962**, *17*, 309–324.
(87) Paz, Y.; Luo, Z.; Rabenberg, L.; Heller, A. Photooxidative Self-Cleaning Transparent Titanium-Dioxide Films on Glass. *J. Mater. Res.* **1995**, *10*, 2842–2848.
(88) Bartolo, D.; Bouamrirene, F.; Verneuil, E.; Buguin, A.; Silberzan, P.; Moulinet, S. Bouncing or Sticky Droplets: Impalement Transitions on Superhydrophobic Micropatterned Surfaces. *Europhys. Lett.* **2006**, *74*, 299–305.
(89) Reyssat, M.; Yeomans, J. M.; Quéré, D. Impalement of Fakir Drops. *Europhys. Lett.* **2008**, *81*, 26006.
(90) Patankar, N. A. Consolidation of Hydrophobic Transition Criteria by Using an Approximate Energy Minimization Approach. *Langmuir* **2010**, *26*, 8941–8945.

(91) Ahuja, A.; Taylor, J. A.; Lifton, V.; Sidorenko, A. A.; Salamon, T. R.; Lobaton, E. J.; Kolodner, P.; Krupenkin, T. N. Nanonails: A Simple Geometrical Approach to Electrically Tunable Superlyophobic Surfaces. *Langmuir* **2008**, *24*, 9–14.
(92) Laermer, F.; Schilp, A. Method of Anisotropically Etching Silicon. 5501893, March 26, 1996.
(93) Leopold, S.; Kremin, C.; Ulbrich, A.; Krischok, S.; Hoffmann, M. Formation of Silicon Grass: Nanomasking by Carbon Clusters in Cyclic Deep Reactive Ion Etching. *J. Vac. Sci. Technol. B Microelectron. Nanometer Struct.* **2011**, *29*, 011002.
(94) Della Volpe, C.; Maniglio, D.; Siboni, S.; Morra, M. An Experimental Procedure to Obtain the Equilibrium Contact Angle from the Wilhelmy Method. *Oil Gas Sci. Technol.* **2001**, *56*, 9–22.